INSTITUTO DE PESQUISAS ENERGÉTICAS E NUCLEARES
Autarquia Associada à Universidade de São Paulo

Retrieval of the planetary boundary layer height in São Paulo from ceilometer and lidar measurements

AMANDA VIEIRA DOS SANTOS

Dissertação apresentada como parte dos requisitos para obtenção do Grau de Mestre em Ciências na Área de Tecnologia Nuclear - Materiais

Orientador:
Prof. Dr. Eduardo Landulfo

São Paulo
2023

INSTITUTO DE PESQUISAS ENERGÉTICAS E NUCLEARES
Autarquia Associada à Universidade de São Paulo

Retrieval of the planetary boundary layer height in São Paulo from ceilometer and lidar measurements

Versão Corrigida

Versão Original disponível no IPEN

AMANDA VIEIRA DOS SANTOS

Dissertação apresentada como parte dos requisitos para obtenção do Grau de Mestre em Ciências na Área de Tecnologia Nuclear - Materiais

Orientador:
Prof. Dr. Eduardo Landulfo

São Paulo
2023

Fonte de Financiamento: CAPES Processo n. 88887.473711/2020-00

Como citar:

SANTOS, A. V. d. ***Retrieval of the planetary boundary layer height in São Paulo from ceilometer and lidar measurements***. 2023. 85 f. Dissertação (Mestrado em Tecnologia Nuclear), Instituto de Pesquisas Energéticas e Nucleares, IPEN-CNEN, São Paulo. Disponível em: ‹http://repositorio.ipen.br/› (data de consulta no formato: dd/mm/aaaa)

Ficha catalográfica elaborada pelo Sistema de geração automática da Biblioteca IPEN, com os dados fornecidos pelo(a) autor(a).

Santos, Amanda Vieira dos
Retrieval of the planetary boundary layer height in São Paulo from ceilometer and lidar measurements / Amanda Vieira dos Santos; orientador Eduardo Landulfo. -- São Paulo, 2023.
85 f.

Dissertação (Mestrado) - Programa de Pós-Graduação em Tecnologia Nuclear (Materiais) -- Instituto de Pesquisas Energéticas e Nucleares, São Paulo, 2023.

1. Planetary Boundary Layer. 2. Remote Sensing. 3. Lidar. 4. Ceilometer. 5. Wavelet Covariance Transform. I. Landulfo, Eduardo, orient. II. Título.

Dedico este trabalho a todos que contribuíram de alguma forma a sua realização,
seja com dados, conhecimento, ou palavras de apoio e incentivo.

Agradecimentos

Agradeços aos meus pais, irmão e amigos, por todo apoio e paciência.

Agradeço aos meus colegas e amigos do IPEN, IAG e IF, especialmente ao orientador Eduardo Landulfo, por todo o conhecimento e ajuda durante os meus anos no mestrado.

Agradeço à CAPES pelo apoio financeiro concedido através da bolsa de mestrado.

“Equipped with his five senses,
man explores the universe around him
and calls the adventure Science.”
Edwin Hubble

RESUMO

Sistemas de sensoriamento remoto são ferramentas poderosas para a realização de medidas atmosféricas. Neste trabalho, é apresentada uma comparação entre dois sistemas de sensoriamento remoto, um lidar e um ceilômetro, na determinação da altura da Camada Limite Planetária (CLP) na cidade de São Paulo com o método *Wavelet Covariance Transform* (WCT). Todos os dados utilizados neste trabalho foram coletados entre fevereiro e dezembro de 2021. Os instrumentos operaram durante o ano de 2021. Os sistemas utilizados foram um lidar elástico (MSP-LIDAR I), que opera em 355 nm, 532 nm e 1064 nm, e um ceilômetro (Lufft CHM 15k *ceilometer*) que opera apenas no infravermelho, em 1064 nm. Os resultados foram comparados em diferentes situações através de estudos de caso, que mostraram boa concordância entre os valores obtidos com os dados de ambos os instrumentos em situações de calmaria. Foram obtidas as alturas médias mensais do topo da CLP entre fevereiro e dezembro de 2021 e a média diurna da PBL, e foi possível observar os ciclos diurno e sazonal da PBL. Os resultados mostraram boa aplicabilidade do ceilômetro para realização de medidas para obtenção da altura do topo da PBL. Uma aplicação dos dados foi apresentada, comparando as alturas obtidas ao longo de 2021 com concentrações de CO_2 medidas em três locais de São Paulo, e os resultados mostraram anti-correlação entre a altura da CLP e a concentração desse gás.

Palavras-chave: Camada Limite Planetária, Sensoriamento Remoto, Lidar, Ceilometer, Wavelet Covariance Transform

ABSTRACT

Remote sensing systems are powerful tools for atmospheric measurements. In this work, a comparison is presented between two remote sensing systems, a lidar and a ceilometer, in determining the height of the Planetary Boundary Layer (PBL) in the city of São Paulo with the Wavelet Covariance Transform (WCT) method. All data included in this work was collected between February and December, 2021. The systems used were an elastic lidar (MSP-LIDAR I), which operates at 355 nm, 532 nm and 1064 nm, and a ceilometer (Lufft CHM 15k ceilometer) which operates only in the infrared, at 1064 nm. The results are compared in different situations through case studies, which show good agreement between the values obtained with the data from both instruments in calm situations. The monthly average PBL top heights between February and December 2021 and the diurnal average of the PBL are obtained, and it is possible to observe the diurnal and seasonal cycles of the PBL. The results show good applicability of the ceilometer for carrying out measurements to obtain the PBL top height. An application of the data is presented, comparing the heights obtained throughout 2021 with CO_2 concentrations measured in three locations in São Paulo, and the results show an anti-correlation between the height of the PBL and the concentration of this gas.

Keywords: Planetary Boundary Layer, Remote Sensing, Lidar, Ceilometer, Wavelet Covariance Transform

List of Tables

List of Figures

List of Abbreviations

CBL	Convective Boundary Layer
CIENTEC	Parque de Ciência e Tecnologia
CLA	Centro de Lasers e Aplicações
CRDS	Cavity Ring-Down Spectroscopy
EZ	Entrainment Zone
FA	Free Atmosphere
IAG	Instituto de Astronomia, Geofísica e Ciências Atmosféricas
IL	Inversion Layer
IPCC	Intergovernmental Panel on Climate Change
IPEN	Instituto de Pesquisas Energéticas e Nucleares
LIDAR	Light Detection and Ranging
ML	Mixed Layer
NBL	Neutral Boundary Layer
PBL	Planetary Boundary Layer
PBLH	Planetary Boundary Layer Height
$PBLH_{ceil}$	PBLH retrieved from ceilometer data
$PBLH_{lidar}$	PBLH retrieved from lidar data
$PBLH_{radio}$	PBLH retrieved from radiometer data
PICO	Pico do Jaraguá station
RL	Residual Layer
RCS	Range Corrected Signal
SBL	Stable Boundary Layer
THLD	WCT threshold
UNI	Universidade Cidade São Paulo - UNICID
UNICID	Universidade Cidade São Paulo
WCT	Wavelet Covariance Transform

List of Symbols

α	Extinction coefficient
β	Backscatter coefficient
c	Speed of light
λ	Wavelength
O	Overlap function
η	System efficiency
P	Power of a laser pulse
τ	Pulse duration

SUMMARY

1 INTRODUCTION

Growing emissions of greenhouse gases (GHGs), such as carbon dioxide (CO_2), methane (CH_4), and carbon monoxide (CO), as well as of other climate pollutants, generate impacts on the planet's atmosphere, life, and economic systems. Industrial processes and the burning of fossil fuels are responsible for most of this increase (IPCC, 2021). The presence of these gases and of short-lived climate pollutants, which include particulate matter, in the atmosphere is responsible for the impacts attributed to climate change. Large cities and power plants play a significant role in these emissions. In the coming years, the number of megacities around the world is expected to continue to grow (UNITED NATIONS, 2014) and, along with this increase, emissions of atmospheric pollutants and greenhouse gases are also expected to intensify, as well as the need to assess the impact of these emissions on the atmosphere and understand their influence on the climate.

São Paulo is the largest megacity in South America, and with a large population and industrial presence, the region is a suitable location for studying the impact of greenhouse gas emissions and pollutants on the atmosphere. Monitoring the presence of these gases and atmospheric pollutants, as well as studying their properties and the processes involved in their transport and dispersion, can be a challenging task, due to the various factors that influence these processes. One of them is the development of the Planetary Boundary Layer (PBL), also called the Atmospheric Boundary Layer, where most of the dispersion of pollutants in the atmosphere occurs.

The atmosphere is divided into layers, extending from its lowest layer, the troposphere, up to the exosphere thousands of kilometers from the Earth’s surface. The surface of the planet, as well as the processes and activities that occur near it, directly influence the lowermost layer of the atmosphere, creating what is called the Planetary Boundary Layer (STULL, 1988). Studies on the PBL benefit from monitoring its dynamics under different conditions, due to the influence of factors that vary with time and location. The depth of the layer varies over time, and it can extend from a few hundred meters to a few kilometers. Much of the aerosol and human pollution is

trapped by the PBL, and it is in this layer where there is the highest concentration of aerosols and where their circulation occurs (STULL, 1988). Processes of transport and dispersion of atmospheric pollutants are substantially associated with air quality control (GARRATT, 1994).

In addition to its important role in aerosol mixing in the atmosphere, the PBL also influences other climate and radiative processes. Solar radiation absorbed by the Earth's surface is transmitted to the atmosphere by processes that occur in the PBL, such as sensible and latent heat fluxes. Radiative transfer processes are also affected by aerosol concentrations in this layer. Cloud formation, which depends on the presence of cloud condensation nuclei and water vapor, is also influenced by processes that occur in the PBL, with this layer having a fundamental role in the occurrence of low clouds (HOLTON et al., 2002). It is also in the PBL where fog formation occurs (STULL, 1988). Thus, climate and meteorology are influenced by the processes that occur in the PBL, also influencing, directly and indirectly, life on the planet (GARRATT, 1994; SEIBERT et al. 2000).

There is a need for a closer monitoring of PBL dynamics, whether for air quality control or for studies on the radiative processes that occur on the planet and how they are influenced by the presence of aerosols and clouds, as well as their impacts on the climate. However, studying the structure of this layer, which has high variability and turbulent behavior, requires the use of systems that can monitor the behavior of the PBL with good spatial and temporal resolution. Remote sensing systems are important allies for boundary layer studies, as they provide measurements of atmospheric variables such as temperature, relative humidity, and aerosol concentrations. With profiles of these atmospheric variables, it is possible to study the structure of the boundary layer, as well as detect the Planetary Boundary Layer height (PBLH), an important parameter for studies on the concentration and dispersion of pollutants (TANG et al., 2015; LI et al., 2017).

The lidar technique is widely used for studies of the atmosphere. The high temporal and spatial resolution of lidar systems allow a detailed study of the PBL top height (KORNOHEN et al., 2014, PAL. et al. 2015; BRAVO-ARANDA et al., 2017). The system works like a light radar, emitting laser pulses and measuring the light returning to the instrument, generating backscatter profiles. Large variations and peaks in these profiles correspond to the presence of clouds or changes in aerosol concentrations in the atmosphere. The possibility of detecting these changes is especially useful for

studies on the PBL, as the layer generally has a higher aerosol concentration than in the free atmosphere. Numerical methods that use this variation to detect the layer height, such as the Wavelet Covariance Transform Method, are used in studies on PBL height around the world (COHN and ANGEVINE, 2000; BROOKS, 2003; DAVIS et al., 2000; GRANADOS-MUÑOZ et al. al., 2012; LOPES et al., 2014).

The ceilometer, an instrument which operates similarly to the lidar by emitting laser pulses to obtain light backscatter profiles, is another remote sensing system that can be used for studies of the atmosphere. This instrument can be used to monitor the dynamics of the PBL, when there is a need for continuous PBL monitoring (MÜNKEL et al., 2007). The ceilometer has a weaker laser source than the lidar, lower maximum range, and presents more noise in its backscatter signal. However, the instrument has the advantages of not needing constant monitoring during its use and having a lower cost than a lidar system. Thus, due to its low cost and easy automation, the ceilometer can be a very useful instrument in the construction of atmosphere monitoring networks. Operating remote sensing instruments at different locations of a city or region can help to observe the variability of the PBL in an urban area, as well as contribute to studies of pollutant concentration and dispersion on the site. Verifying the efficiency of this instrument for PBL studies compared to more powerful lidar systems is therefore an important step for its use in future studies.

2 OBJECTIVES

This work aims to present an intercomparison of results obtained through the use of data from a lidar system and a ceilometer operating at two different locations in the city of São Paulo, and show the efficacy of using data from these instruments to retrieve the Planetary Boundary Layer height by using the Wavelet Covariance Transform Method, as well as to use this data to study the daily and seasonal Planetary Boundary Layer height variability in the city, and present an application of the results by comparing them with CO_2 concentrations obtained in the same time frame used in the study.

3 LITERATURE REVIEW

In this section, the following themes will be discussed: the Planetary Boundary Layer; CO_2 and CH_4 emissions and their impact on climate change; remote sensing systems for the study of the Planetary Boundary Layer height; and numerical methods commonly used to determine the PBLH.

3.1 The Planetary Boundary Layer (PBL)

The Earth's atmosphere is divided into layers based on temperature changes with altitude. Each layer has its own temperature and pressure profile, as seen in Figure 1. Its lowest layer, the troposphere, is in direct contact with the Earth's surface and, as such, is the layer of the atmosphere that is directly influenced by natural and anthropogenic processes and activities that occur near the surface.

Figure 1: Temperature profile of the atmosphere as a function of height and pressure.

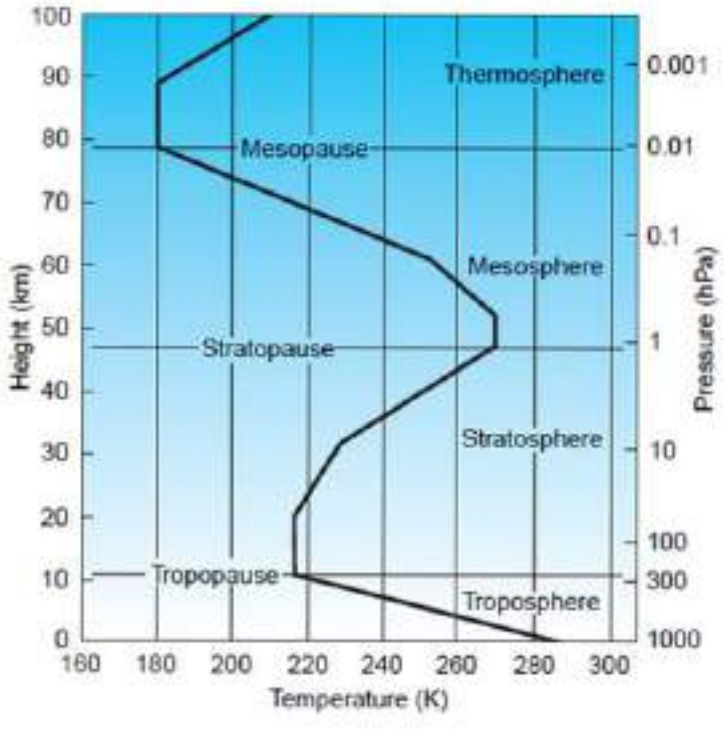

Source: adapted from Wallace and Hobbs, Atmospheric Science - an Introductory Survey, Academic Press, 2006.

The planetary boundary layer is defined as the layer of air directly above the surface of the planet which is subjected to the impact of surface forcings in time scales of an hour or less (STULL, 1988). This layer constitutes the lowermost region of the troposphere and is defined by the interactions happening between the atmosphere and the surface, such as heat fluxes, evaporation and transpiration, pollutant emissions, clouds, surface friction, among other factors. The depth of this layer varies from a few hundred meters up to a few kilometers, variying during its diurnal cycle and showing spatial and temporal variability. The PBL has an important role on the behavior of the atmosphere, influencing heat and humidity exchanges between the surface and the free atmosphere above it. The PBL also influences pollutant dispersion, as well as the formation of low clouds, hence also affecting the radiation balance on the surface (STULL, 1988). It also has an important role in air quality, as the PBL top height defines the volume in which the pollution is distributed, affecting pollutant concentration near the surface. Studying the PBL is important for many areas of the atmospheric sciences, such as climate modelling, weather forecasting and studies on pollutant transport, dispersion, and air quality (SEIBERT et al., 2000; MEDEIROS et al., 2005).

A notable characteristic of the PBL is its turbulent behavior, and its variability usually presents a diurnal and seasonal cycle influenced by variations in factors such as air temperature near the surface, air density, relative humidity, radiative fluxes, local topography, winds, and atmospheric stability. These forcings drive diurnal growth and collapse of the Convective Boundary Layer. During the day, the heat flux generated by solar radiation causes an increase in air temperature near the surface, generating convective processes that expand the PBL. At night, the negative radiative flux causes surface cooling, leading to a reduction in convective activity and decreasing turbulent exchanges between the atmosphere and the surface. Due to diurnal variation in PBL characteristics, the layer can be classified in three main types: the Stable or Nocturnal Boundary Layer (SBL), formed when heat fluxes are negative, that is, directed from the atmosphere to the surface; the Neutral Boundary Layer (NBL), formed when heat fluxes near the surface are close to zero; and the Convective Boundary Layer (CBL), formed when heat fluxes are positive, that is, directed from the surface to the atmosphere (STULL 1988, LIU and LIANG, 2010).

During the day, the PBL has a daily cycle that goes through the previously mentioned types and, between these main cycles, there are also transition regions that

are formed due to surface-atmosphere interactions. These regions are discussed in greater detail in the following sections.

Figure 2: Typical diurnal evolution of the planetary boundary layer.

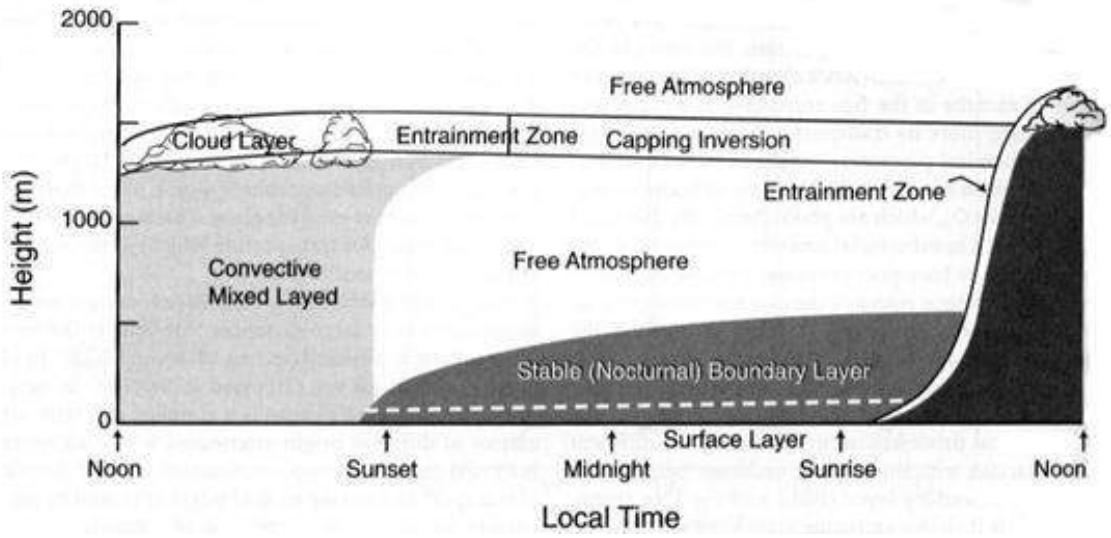

Source: adapted from Stull, Boundary Layer Meteorology, Kluwer, 1988.

3.1.2 Convective Boundary Layer (CBL)

The CBL usually forms during daytime and its height varies in response to the ascension of air parcels due to surface heating (EICHINGER et al., 2005). With increased solar radiation incidence on the surface during daytime, there is a change in heat fluxes, which are now positive, with the surface warmer than adjacent air. The vertical development of the CBL is driven by the formation of convective processes caused by the latent and sensible heat fluxes, where heated air masses rise in the atmosphere as they become denser. The CBL presents strong turbulence which leads to well-mixed potential temperature profiles (STULL, 1988).

This layer is defined as unstable since it presents negative variation in its potential temperature profile θ_v:

$$\frac{\partial \theta_v}{\partial z} < 0$$

The CBL usually follows a predictable pattern, emerging right after sunrise, with its growth being initiated by the convection process generated by the sensible heat flux at the surface, reaching its maximum height usually during early or mid afternoon. However, its duration and growth during the day do not depend only on solar

radiation, but also on geographical and meteorological factors such as the characteristics and topography of the surface, sea breezes, wind, advection and precipitation (BIANCO et al., 2011). For that reason, the PBL usually does not present a structure exactly as idealized.

In well-defined PBLs, CBL growth depends on the rate in which energy is introduced in the PBL by heat fluxes (EICHINGER et al., 2005), and its diurnal evolution and maximum height depend on the sensible heat flux and its stability on the free atmosphere (STULL, 1988).

The CBL is tipically divided in three main layers: the Surface Layer (SL), the Mixed Layer (ML) and the Entrainment Zone (EZ).

The Surface Layer is usually situated in the lower 100 m of the PBL. This layer presents the highest temperature, humidity, and wind speed gradients. Winds in this layer are usually influenced by ground friction and by the vertical temperature gradient. The SL is characteristically turbulent, with significant exchanges of heat, mass and momentum, influencing the entire PBL (KAIMAL and FINNIGAN, 1994). Virtual potential temperature profiles in the SL are often superadiabatic adjacent to the ground (STULL, 1988).

Above the Surface Layer sits the Mixed Layer, the deepest layer in the PBL. Turbulence in this layer is driven by convection, which usually originates from heat exchanges with the ground that cause warm air to rise. In the presence of clouds, radiative cooling at the top of the cloud layer can also be a source of convection, making cold air descend. At the top of the ML, turbulence can also be generated by wind shear. In days when the air parcels rise up to their lifting condensation level (LCL), clouds can be formed if there is enough humidity. In cloudy days, insolation at the surface is decreased which in turn decreases turbulence in the layer and can slow its growth (STULL, 1988). In homogeneous surfaces, turbulent heat transfer and mixing is predominantly vertical (WANG and BRAS, 1998). In the middle portion of the ML, virtual potential temperature profiles are nearly adiabatic (STULL, 1988).

The Entrainment Zone (EZ) is the region of the CBL located between the Mixed Layer and the Free Atmosphere. In this region, free tropospheric air is entrained into the PBL (WALLACE and HOBBS, 2006), usually bringing dryer and warmer air into the ML. Pollutant entrainment to the FA occurs with turbulent mixing during the development of the CBL until turbulence decreases at night. Rapid CBL growth can contribute to the entrainment and transport of gases and pollutants between the PBL

and the FA. The Free Atmosphere is not directly influenced by surface friction and usually presents lower concentrations of particulates and aerosols.

Near sunset, with decreasing incident solar radiation, sensible heat fluxes at the surface also decrease. The CBL decays with the weakening convective processes and turbulence. There is still a residual weak turbulence, constituing a region know as the Residual Layer (RL) (WALLACE and HOBBS, 2006), which maintains some of the characteristics of the ML and remains during nighttime, with its lowermost part becoming the SBL. In the absence of large-scale sinoptic influences, the RL usually remains until sunrise the next day. This layer retains the previous day's pollutants during nighttime and early morning, until it is entrained by the emergence of a new ML (STULL, 1988). Idealized daytime vertical profiles of mean virtual potential temperature, wind speed, water vapor mixing ratio, and pollutant concentration c in the CBL can be seen in Figure 3.

Figure 3: Typical daytime vertical profiles of mean virtual potential temperature $\overline{\theta_v}$, wind speed $\overline{M}$, water vapor mixing ratio $\bar{r}$, and pollutant concentration $\bar{c}$.

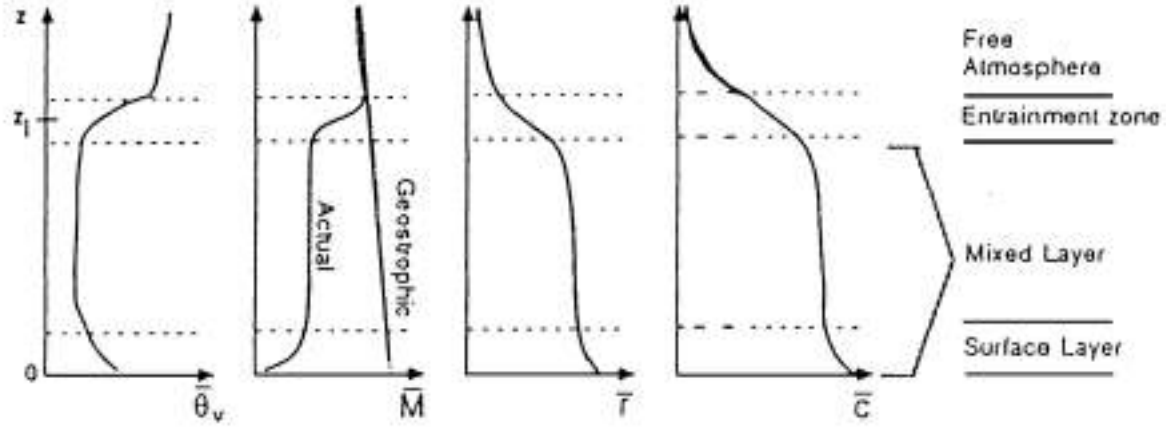

Source: adapted from Stull, Boundary Layer Meteorology, Kluwer, 1988.

3.1.2 Stable Boundary Layer (SBL)

The Stable Boundary Layer usually forms at night, with surface radiative cooling due to the decrease in incident solar radiation. The surface becomes cooler than the adjacent air layer, which leads to this layer losing heat to the surface and the heat flux becomes negative. As the layer of air above the surface becomes cooler, it becomes denser, and the SBL is formed (STULL, 1988).

The intensity of turbulent exchanges between the atmosphere and the surface is weak in the SBL (STULL, 1988). This layer is marked by its stability, which can be observed through its virtual potential temperature profile, with:

$$\frac{\partial \theta_v}{\partial z} > 0$$

Unlike the CBL, the SBL presents small heat fluxes and is a very thin layer, usually not surpassing a few hundred meters at most, or possibly even thinner, with a depth of under 100 m, at clear conditions and light winds (GARRATT, 1994)

The SBL can be divided into three parts. Its lowermost part is equivalent to the Surface Layer, having a depth of only a few meters and being marked by the radiative exchange between the surface and the adjacent air. Above this region, the SBL is marked by turbulent cooling, with potential temperatures changing almost linearly. This region comprises most of the SBL. In the uppermost region of the SBL, there is a layer similar to the EZ called the Inversion Layer (IL). This layer presents high stability, predominantly radiative cooling, and its turbulence decreases with height. Due to the high stability of this layer, there is little vertical pollutant dispersion, which can prevent these pollutants from escaping to the Free Atmosphere (STULL, 1988), and increase pollutant concentrations in the lowermost regions of the SBL. In figure 4, idealized mean virtual potential temperature and wind speed profiles in the SBL are shown.

A Stable Boundary Layer can also form during the day, in situations where the surface is colder than adjacent air, such as, near the coast or during a passage of a hot air mass (STULL, 1988).

During the transition from the SBL to the CBL, the heat flux varies from negative to positive, going through periods in which it is nearly zero. During these periods, the PBL can be classified as a Neutral Boundary Layer (STULL, 1988; MAHRT et al., 1998).

Figure 4: Idealized mean virtual potential temperature and wind speed profiles in the SBL.

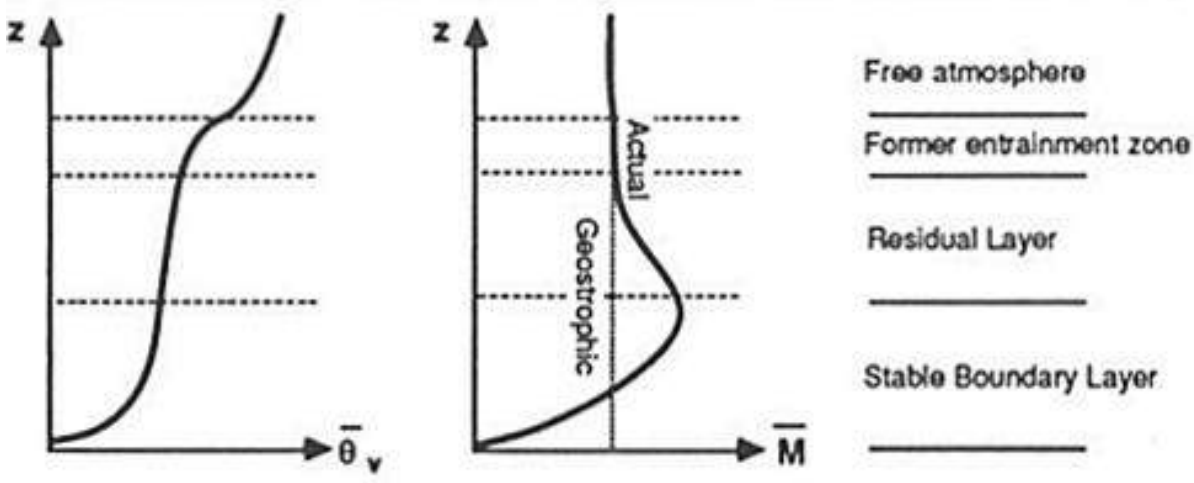

Source: adapted from Stull, Boundary Layer Meteorology, Kluwer, 1988.

3.2 Greenhouse Gases

Changes in greenhouse gas (GHG) concentrations are unequivocally linked to climate change (BALLANTYNE et al., 2012; HODNEBROG et al., 2020, IPCC, 2021). A more intense water cycle and rainfall, amplified permafrost thawing and melting of glaciers, ocean acidification and reduced oxygen levels in the ocean are some examples of how climate change can affect every region of the planet in many aspects. Cities can be more affected by some aspects of climate change, with amplified changes in heat, heavier precipitation and sea level rise (IPCC, 2021).

Since 1850-1900, GHGs emitted by anthropogenic activities have caused a warming of 1.1 °C, and it is expected that the global temperature will continue to rise another 1.5 °C or more over the next 20 years (IPCC, 2021). Changes in global surface temperature relative to 1850-1900 are shown in Figure 5. Carbon dioxide (CO_2) and methane (CH_4) are the two most important contributors to climate change caused by human activities (UNEP, 2018; IPCC 2021). According to a report released by the Intergovernmental Panel on Climate Change (IPCC) in August, 2021, CO_2 and CH_4 concentrations in the atmosphere have continued to rise since around 1750, reaching annual averages of 410 ppm and 1886 ppb respectively (IPCC, 2021).

Figure 5 – History and causes of global temperature change.

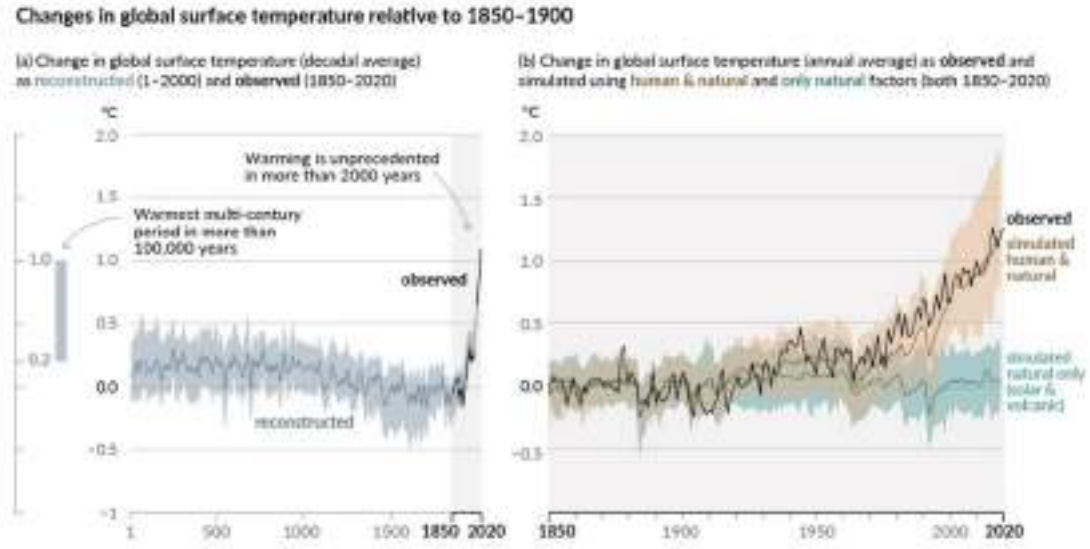

Source: IPCC, Summary for Policymakers, Cambridge University Press, 2021.

Carbon dioxide is a long-lived anthropogenic GHG. It accounts for about 66% of the warming effect on the climate (WMO, 2021). From 1990 to 2020, there was an increase of 47% on the radiative forcing by long-lived GHGs, and most of this increase, about 80%, can be attributed to CO_2 (WMO, 2021). The main sources of global anthropogenic CO_2 emissions are fossil fuel combustion, cement production flaring and land use. About 78% of the increase in GHG emissions in the 1970-2010 period can be attributed to fossil fuel combustion and industrial processes (IPCC, 2014). Diurnal CO2 fluxes are strongly linked to vehicular traffic. A time series of the global anthropogenic CO2 emissions is shown in figure 6.

Figure 6 - Global CO2 emissions from anthropogenic activities (left-hand side) and cumulative CO2 emissions (right-hand side).

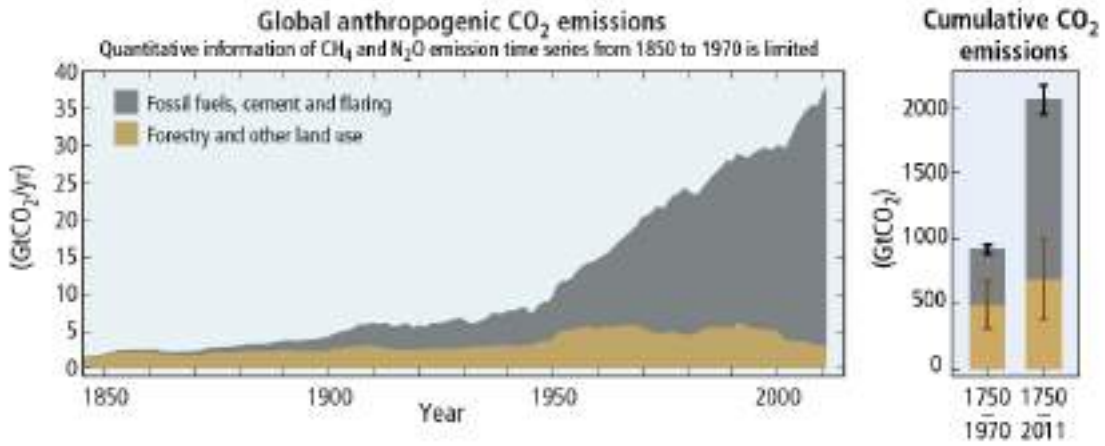

Source: IPCC, Climate Change 2014: Synthesis Report.

Land and oceans are the main CO_2 sinks, taking up about 56%, globally, of emissions from human activities per year (IPCC, 2021), while the remaining atmospheric CO_2 contributes to climate change (IPCC, 2014). How much CO2 remains in the atmosphere is an important indicator of the sources/sinks balance.

CH_4 is responsible for approximately 20% of the global warming caused by all well-mixed greenhouse-gases (RAMANATHAN et al., 1985; IPCC, 2014, 2021). The increase in atmospheric CH_4 can cause substantial impact on the climate. Much of the thermal infrared radiation emitted by the planet is absorbed by atmospheric methane. Therefore, this greenhouse gas has important radiative forcing potential (MYHRE et al., 2013). Tropospheric ozone (O_3), another greenhouse gas that is an important contributor to climate change (UNEP, 2018), is also produced by CH_4. Although CH_4 concentrations are smaller than that of CO_2, the Global Warming Potential of CH_4 is larger than that of CO_2 (KIRSCHKE et al., 2013; VOULGARAKIS et al., 2013). Thus, it is important to understand the impact of atmospheric CH_4 on the Earth's climate, and monitor its sources and sinks, as well as its global distributions and long-term trends in future years. CH_4 is emitted to the atmosphere by anthropogenic and natural processes (KIRSCHKE et al., 2013). Approximately 60% of CH_4 emissions are due to anthropogenic sources, such as coal, oil and gas production and consumption, agriculture and waste, while about 40% are emitted by natural sources, such as wetlands, termites, gas-oil seeps, wild animals, methane hydrates, permafrost and oceans (KIRSCHKE et al., 2013). Most of the uncertainty related to the CH4 budget in the atmosphere is due to its natural sources. CH_4 emitted by natural sources has remained virtually unchanged over the past twenty years, while most of the increase in methane concentrations have been caused by anthropogenic emissions (JACKSON et al., 2020).

Figure 7: Locations of current and projected megacities between 2018 and 2030.

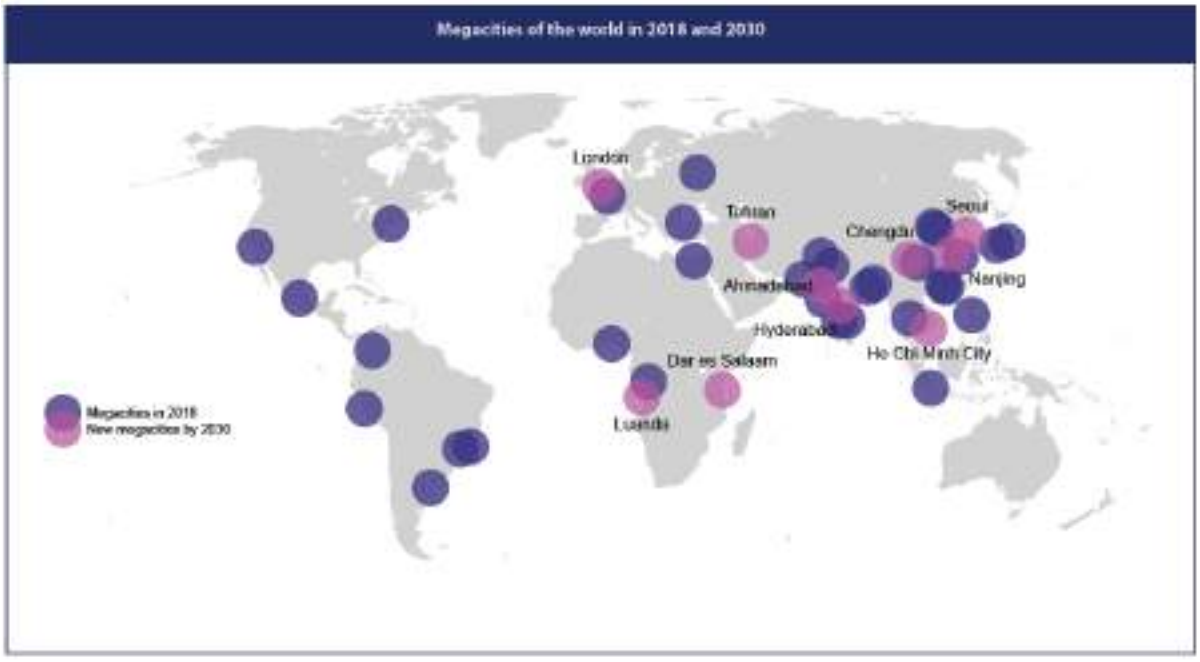

Source: United Nations, The World's Cities in 2018 – Data Booklet, 2018.

A strong reduction in GHG emissions still has the potential to limit climate change. Net zero CO_2 and reduced CH_4 emissions would significantly slow down the rate of warming (IPCC, 2021). Figure 7 shows the locations of current and projected megacities in the world. Cities, and especially megacities, contribute a significant amount of GHG emissions, accounting for approximately 70% of CO_2 anthropogenic emissions (CANADELL et al., 2010), and understanding this contribution is important for the creation of mitigation policies and strategies. However, estimating these emissions can be a complicated task, as they are influenced by not only anthropogenic activities but also land-surface interactions.

Estimating the spatiotemporal distribution of GHGs is a complex process, but it is possible to estimate the concentration of recently emitted gases near the surface. Measuring GHG concentrations in the PBL can be a useful tool to study GHG sinks and sources, as well as monitor trends. GHG concentrations and PBL height present a lot of diurnal variation. Therefore, accurately estimating the PBL height is crucial and frequent measurements are necessary. CO_2 concentrations are affected by near-surface interactions, such as photosynthesis and respiration, and processes related to PBL dynamics (KIM and VERMA, 1990; JACOBS and de BRUIN, 1992). The morning CO_2 budget is greatly affected by entrainment processes (CULF et al., 1997;

ARELLANO et al., 2004), and diurnal concentrations near the surface are also influenced by turbulence and advection (EUGSTER and SIEGRIST, 2000).

3.3 Retrieval of PBL height from remote sensing data

Studies involving aerosol concentrations or atmospheric dynamics will very often use PBL height data. This height cannot be measured directly, but it can be determined by the detection of changes in some atmospheric variables, such as aerosol concentrations, wind speed, potential temperature and relative humidity. The retrieval of these variable profiles can be made with instruments working in-situ (such as radiosondes) or by remote sensing. PBLHs derived from radiosoundings are commonly estimated from methods such as the Richardson number method (MENUT et al., 1999) using radiosounding wind and temperature profile data. Although these estimates are usually accurate, radiosondes provide sparse data and, as such, are not adequate for detecting the PBLH with high temporal resolution. Remote sensing instruments commonly used for PBLH retrievals are elastic lidars, ceilometers, Doppler wind lidars (MOREIRA et al., 2018), wind-profiling radars (COHN and ANGEVINE, 2000), microwave radiometers (CIMINI et al., 2013). Changes in profiles derived from data obtained with these instruments are used as parameters to detect the transition between the PBL and the Free Atmosphere by different mathematical methods (STULL, 1988). Studies carried out in the last decades suggest that a combination of different remote sensing techniques allow for better PBL development observations (DAYAN and LIFSHITZ-GOLDEN, 2002; COHN and ANGEVINE, 2000; EMEIS et. al, 2008).

Lidar data can be used to detect the PBL top height with precision (MENUT et al, 1999; WIEGNER et al., 2006; MARTUCCI et al, 2007). The presence of a greater aerosol concentration in the PBL can be seen as a region of high backscattering in comparison with the region directly above it. This abrupt change from high to low backscattering represents the region where the PBL top can be identified by some numerical methods. Many lidar-based PBLH detection mathematical algorithms depend on the decrease in lidar signal strength with height, searching for strong decreases associated with the top of the boundary layer (MENUT et al., 1999; PAL et al., 2010). For lidar data, a few of the most used methods are the Wavelet Covariance Transform Method (COHN and ANGEVINE, 2000; DAVIS et al., 2000; BROOKS, 2003; GRANADOS-MUÑOZ et al., 2012; LOPES et al., 2014), the Gradient Method

(HAYDEN et al, 1997; FLAMANT et al., 1997; MENUT et al., 1999; MARTUCCI et al., 2007; BAARS et al., 2008; LI et al., 2017), the Variance Method (HOOPER and ELORANTA, 1986; PIIRONEN and ELORANTA, 1995; MENUT et al., 1999; MARTUCCI et al., 2007; CAICEDO et al. 2017).

Lidar systems have the advantage of having a long range, being able to detect aerosol layers dozens of kilometers high, and having good spatial and temporal resolutions, as well as little signal noise. However, the system needs a local operator and is not usually able to operate under rain. The ceilometer, an instrument similar to the lidar, does not need constant maintenance and is also easily automated. It is a simple, low-cost instrument, which can be used to detect clouds and to obtain aerosol profiles. Studies have shown that the instrument can also be used to the detect the PBL height (PENG et al., 2017), and the common algorithms of PBLH estimation can also be applied for ceilometers (HAEFELLIN et al., 2012). The instrument is also useful for monitoring aerosol such as volcanic ash (HAEFELE et al., 2017). Due to their lower operational cost, ceilometers can be implemented in remote sensing networks for automatic PBLH measurements. Continuous PBLH monitoring is essential for understanding the transport, mixing and accumulation of aerosols and contaminants. Identifying the situations in which a ceilometer can be used is therefore important to reduce costs and expand monitoring of the lower troposphere structure.

3.4 The lidar technique

Lidar, originally an acronym for Light Detection and Ranging, is a remote sensing technique that works like a light radar, emitting laser pulses that are scattered in all directions in the atmosphere and measuring the backscattered light, i.e., the light returning to the instrument. It is an important instrument for research of the atmosphere and can be used to characterize the vertical distribution of aerosols (DAVIS et al., 2000; LI et al., 2017), as well as for the analysis of its properties, and also for the detection of clouds and measurement of other atmospheric variables (WEITKAMP, 2005), allowing the retrieval of profiles of volumetric backscattering coefficient, volumetric extinction coefficient and depolarization rate (KOVALEV and EICHINGER, 2004). The laser pulse emitted by the instrument is scattered in all directions due to the presence of molecules, aerosols, and clouds in the atmosphere. Part of this signal returns to the instrument, and this backscattered signal is collected by a telescope and measured by a photodetector as a function of distance from the lidar (KOVALEV and EICHINGER,

2004). To detect the presence of clouds and aerosols, an elastic lidar is commonly used. This type of lidar measures light that has been backscattered with the same emitted wavelength (WEITKAMP, 2005).

An overview of a lidar system is presented in Figure 8.

Figure 8: Overview of a lidar system.

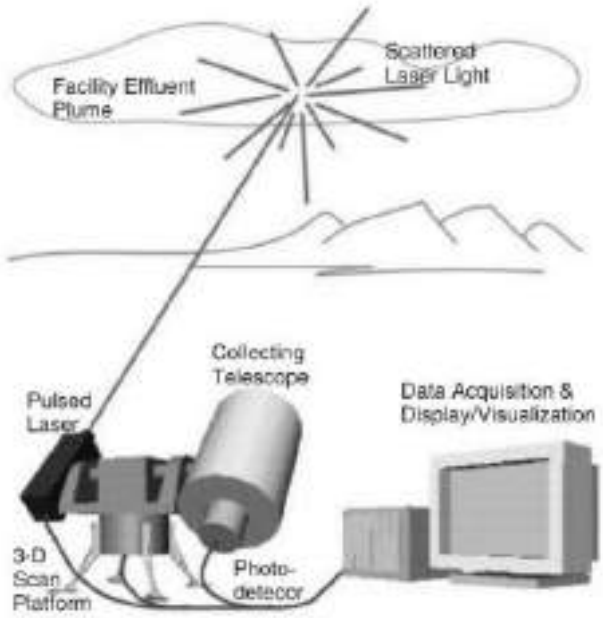

Source: Chapter 3 – Fundamentals of the Lidar Technique, Elastic LIDAR - Theory, Practice and Analysis Methods, Kovalev, V. A. and Eichinger, W. E. John Wiley & Sons, 2004.

The instrument consists of a transmitter, a receiver, and a detector. The transmitter consists of a laser that emits pulses with a wavelength that can vary between approximately 250 nm and 11 μm, depending on the purpose for which the instrument is being used. The pulses have a duration of nanoseconds and are emitted with a repetition frequency of 10 Hz to 5 kHz. The receiver consists of a telescope, which has the role of collecting backscattered light. The system is considered mono-axial if the optical axis of the telescope is coincident with the laser, and bi-axial if it is parallel. The detector converts the light collected by the telescope into electrical signals, through photomultipliers, and digital signals (ADC, analog to digital converter).

The distance at which a lidar can measure varies from instrument to instrument and depends on a combination of system-specific geometric factors. This distance depends on the overlap function, or simply overlap, which is defined by the field of view of the telescope used and the positioning of the emitter and receiver axes (WEITKAMP, 2005). Systems that work on more than one wavelength can be altered by using filters that allow only the light of the wavelength of interest to be measured. It

is also possible to change the signal-to-noise ratio of the signal obtained by the instrument by changing the telescope's field of view (WEITKAMP, 2005).

The equation that describes the signal received by an elastic lidar, $P(R,\lambda)$, that is, the power, is shown below, according to the notation by WEITKAMP (2005).

$$P(R,\lambda) = P_0 \frac{c\tau}{2} A\eta \frac{O(R)}{R^2} \beta(R,\lambda) exp\left[-2\int_0^R \alpha(r,\lambda)dr\right] \quad (1)$$

Where:

- $\beta(R,\lambda)$ is the backscatter coefficient of laser light, with $\beta(R,\lambda) = \beta_{mol}(R,\lambda) + \beta_{aer}(R,\lambda)$, where β_{mol} corresponds to molecular scattering and β_{aer} to scattering by aerosol particles.
- $exp\left[-2\int_0^R \alpha(r,\lambda)dr\right]$ corresponds to extinction, that is, the fraction of light that is lost during the path, with $\alpha(R,\lambda) = \alpha_{mol}(R,\lambda) + \alpha_{aer}(R,\lambda)$, where α_{mol} corresponds to molecular extinction and α_{aer} to extinction due to aerosol particles.
- $\frac{O(R)}{R^2}$ is a geometric factor that includes the overlap function and the quadratic decay of the signal with distance.
- $P_0 \frac{c\tau}{2} A\eta$ is a system-dependent factor, with P_0 being the average power of a laser pulse, τ the pulse duration, c the speed of light, A the area of the receiver collecting backscattered light, and η the system efficiency.

(WEITKAMP, 2005).

The ceilometer is an instrument that was developed for the detection of the altitude of clouds in airports. Its working principle is similar to that of a lidar, but the instrument operates on only one wavelength and usually has a weaker laser source, resulting in a shorter instrument range and noisier signal.

3.5 Cavity Ring-Down Spectroscopy

Cavity Ring-Down Spectroscopy (CRDS) is a direct absorption technique used to make precise trace gas measurements (BITTER et al., 2005; CROSSON, 2008), using pulsed or continuous light sources. It has a better sensitivity than other techniques such as conventional absorption spectroscopy. It can provide the gas concentration of a gas by determining the optical absorbance of a gas sample in a closed high-finesse optical cavity (CROSSON, 2008).

Basic CRDS spectrometers are composed of a laser, a high finesse optical cavity with two or more mirrors and a photodetector (CROSSON, 2008). It works by monitoring the built-up intensity of laser light injected into the cavity with a photodetector. The laser is quickly turned off and the light intensity inside the cavity is measured as it decays. The light remains trapped in the cavity for a long period of time and the length of this process depends on the absorption and scattering characteristics of the sample being analyzed, as well as the cavity mirrors used (CROSSON, 2008).

4 MATERIALS AND METHODS

Data from a lidar system and a ceilometer was used to obtain the PBLH in 2021. The lidar system operated a few days a month during the year. A commercial ceilometer was in continuous operation from February to December, 2021. Backscatter profiles obtained with these instruments were used to calculate the PBLH at two points in the city of São Paulo using the Wavelet Covariance Transform Method.

The lidar system used in this work, the MSP-LIDAR I, operates at the Center for Lasers and Applications (CLA) of the Energy and Nuclear Research Institute (IPEN). A CHM 15k ceilometer operates approximately 11 km away, at the CIENTEC Park.

CO_2 concentrations were obtained with Picarro CRDS Spectrometers located at different locations in the city.

The following tasks are carried out in this work:

- Obtaining backscattering data with two different systems in different locations in the city;
- Apply a numerical method to obtain the PBLH with the instrument data;
- Comparing the results obtained by the instruments;
- Checking the dynamics of the PBLH over the months during the measurement period;
- Comparing the results to greenhouse gases concentrations such as CO2 and CH4 in the city of São Paulo.

This work is linked to the METROCLIMA-SP project, whose goal is to study the role of emissions by the megacity of São Paulo on air quality and regional climate change. The project has researchers and collaborators at several national and international universities and institutions, and its coordinator is Professor Maria de Fátima Andrade (IAG-USP). The ceilometer and CRDS analyzers used in this work are part of the METROCLIMA-SP project.

4.1 Methods

4.1.1 Wavelet Covariance Transform (WCT)

The Wavelet Covariance Transform method algorithm was applied to the data, with a few adaptations to improve retrieval in different conditions. This method was chosen because it has shown good applicability under different meteorological conditions and allows for adjustability.

The aerosol concentration in the PBL is usually distinctly greater than in the free atmosphere. The WCT method can be used to obtain the PBL top height from lidar data, identifying changes in the concentration of aerosol through the detection of step changes in the range-corrected signal (BAARS et al., 2008). The step change in the lidar backscatter signal is similar to the step change of the Haar wavelet function. The similarity between the RCS and the Haar function is measured by the covariance transform $W_f(a,b)$. It is defined by the equation:

$$W_f(a,b) = \frac{1}{a}\int_{z_b}^{z_a} RCS(z)h\left(\frac{z-b}{a}\right)dz \quad (2)$$

Where $h\left(\frac{z-b}{a}\right)$ corresponds to the Haar function, expressed as:

$$h\left(\frac{z-b}{a}\right) = \begin{cases} -1: b - \frac{a}{2} \le z \le b \\ 1: b \le z \le b + \frac{a}{2} \\ 0: Other\ cases \end{cases}$$

In the equation, RCS is the range-corrected signal $P(z)z^2$, z_a and z_b are the lower and upper limits of the signal, a is the dilation of the function and b the vertical translation of the function (BROOKS, 2003).

Figure 9: Representation of the Haar function, h, dilation *a* and translation *b*.

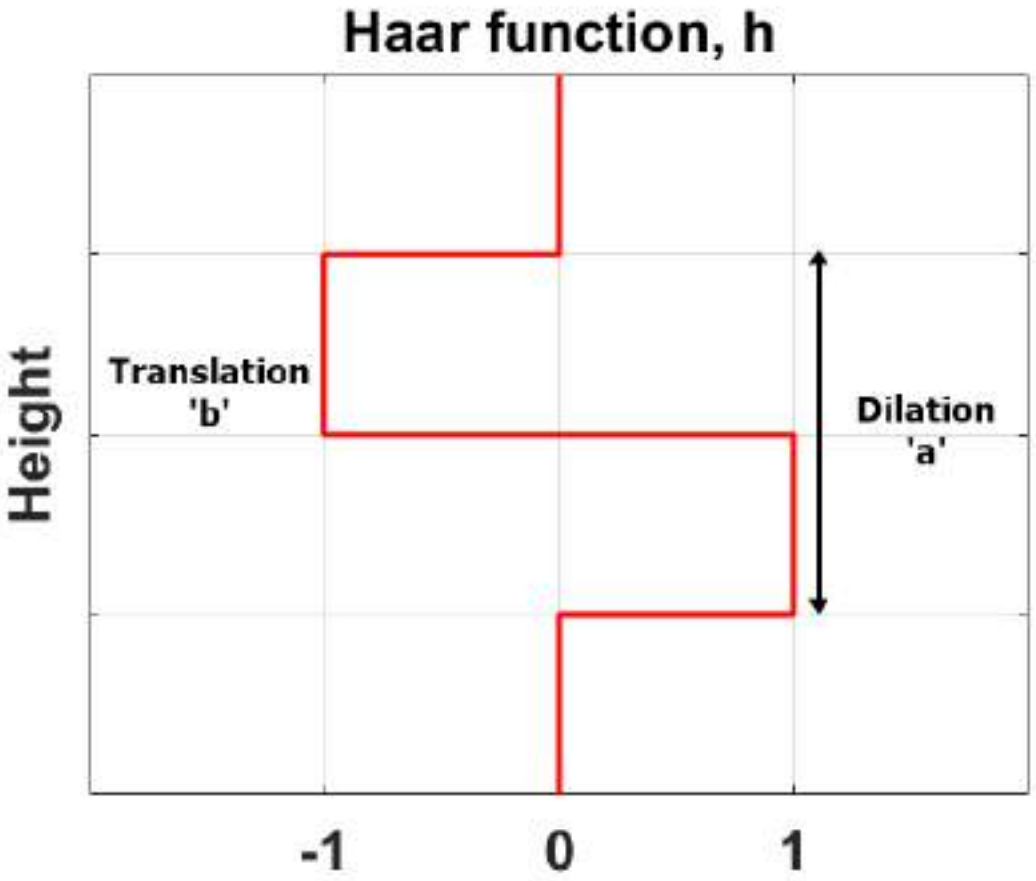

Source: author, 2023.

The global maximum value taken by $W_f(a, b)$ corresponds to the height in which an abrupt change is seen in the lidar signal, as it represents the location where the backscatter profile and the Haar wavelet function present greatest similarity.

Before obtaining the covariance transform, it is necessary to define the initial conditions *a* and *b*. Choosing the appropriate initial conditions is crucial for accurately determining the PBLH. The dilation of the Haar function, *a*, defines the extent of the step function, i.e. where the algorithm is looking for an abrupt change in the profile. For better results, the value of *a* should be large enough to contain the extent of the transition zone. Too small values of *a* can result in the detection of small gradients corresponding to aerosol layers, low clouds and noise, generating multiple local maxima, while large values of *a* can reduce the precision in determining the PBLH. In non-ideal conditions, the appropriate selection of *a* is necessary for an accurate retrieval of the PBLH. In ideal conditions, the selection of *a* is not as critical, as the local maxima are not as affected by the value of *a*. The value of *b* corresponds to the

center of the Haar function. As *b* translates the location where the function is centered, this translation should not be greater than the value of *a*. Figures 10 and 11 show lidar RCS and WCT profiles and the effect of changing the values of *a* in the WCT profile.

Figure 10 - RCS and WCT profiles obtained on May 19th, 2021 from 30-minute averaged data between 17:11 and 17:40 UTC (left-hand side) and the *W(a,b)* profiles obtained using different values of *a* (right-hand side).

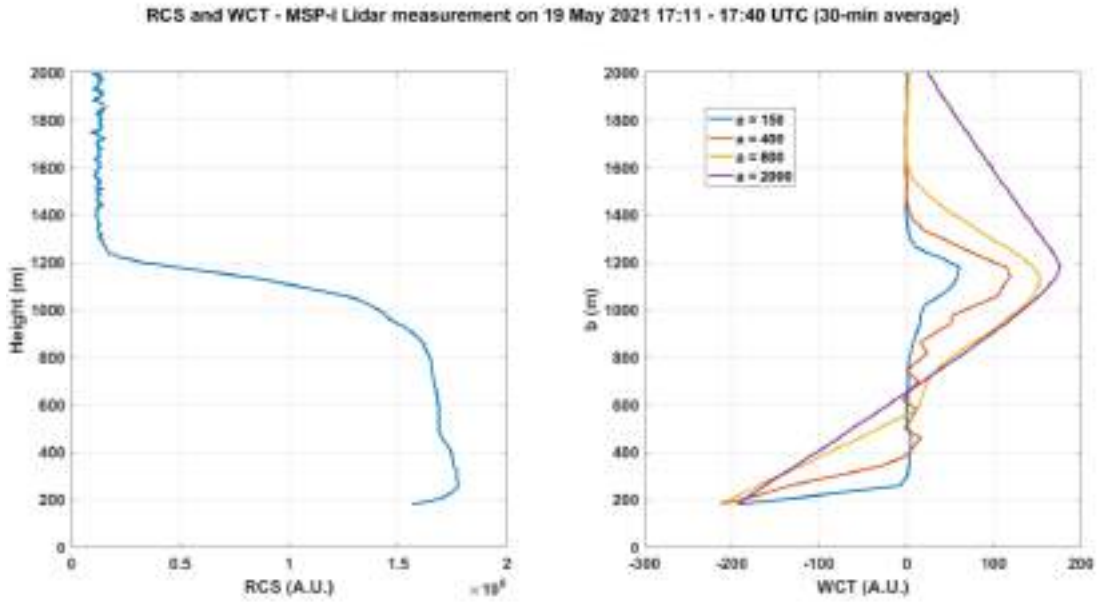

Source: author, 2023.

Figure 11 - RCS and WCT profiles obtained on September 14th, 2021 from 30-minute averaged data between 15:10 and 15:40 UTC (left-hand side) and the *W(a,b)* profiles obtained using different values of *a* (right-hand side).

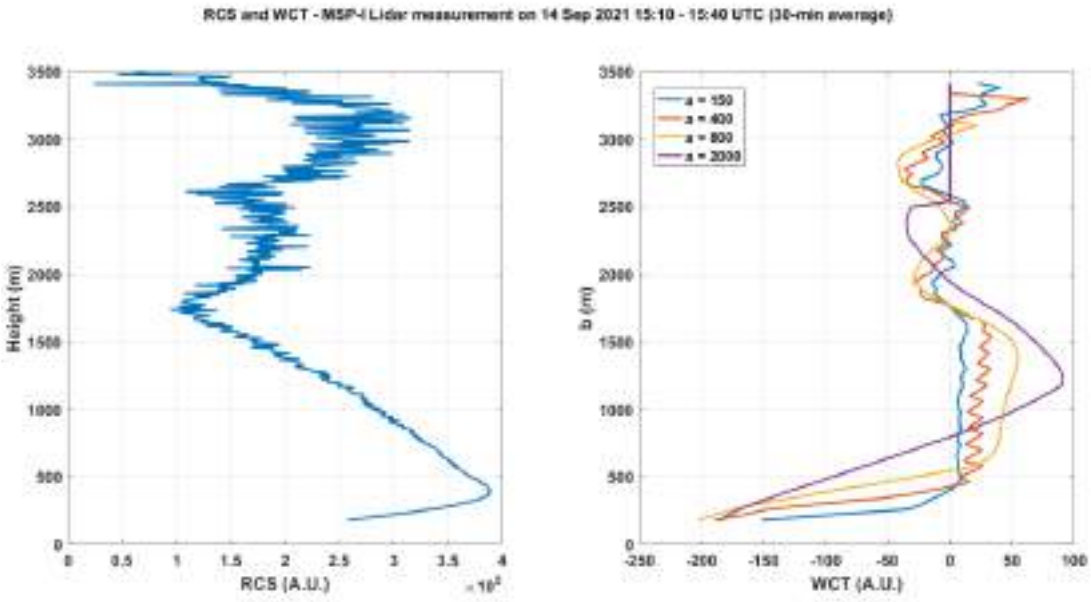

Source: author, 2023.

The WCT method has the advantage of being able to be applied in complex cases (DAVIS et al., 2000), being less affected by noise and being easily automatized (BAARS et al., 2008), since its *a* and *b* parameters can be adjusted to better identify the PBL height in different situations. However, when there are multiple aerosol layers, the accuracy of the method can be affected (TANG et al., 2016).

A few adaptations and conditions were applied to improve the accuracy of the results. The CHM 15K ceilometer provides estimates of cloud base heights for each of its signal profiles. Although results are obtained automatically and sometimes present errors, this information is useful to screen the profiles included in the analysis for the presence of low clouds that could interfere with the PBLH retrieval. Each profile where the ceilometer detected a cloud at a height lower than 2500 m was excluded from the analysis, as well as its two neighboring profiles. The instrument also provides information on window visibility. Profiles with very low window visibility are usually indicative of rain and were removed from the analysis. The CHM 15k's backscattering signal can present high noise during daytime and in the presence of thick or multiple cloud or aerosol layers due to attenuation of the signal. In order to improve signal-to-noise ratio and better identify changes in the signal, a 30-minute average was applied to the backscatter profiles. At nighttime, the algorithm searched for PBL heights up to 500 m. The results were analyzed for unexpected changes of PBL height, such as abrupt peaks. In order to improve the accuracy of the results, a 4 or 5-point moving average was used instead in some cases.

4.2 Locations

São Paulo (23°33'S, 46°38'W, 760 m a.s.l.) is the most populous city in Brazil, the Southern Hemisphere and the Americas. The city has an estimated population of over 12 million, and the Metropolitan Area of São Paulo (MASP) has a population of around 21 million (IBGE, 2021). The city's large population and industrial presence contribute to large anthropogenic emissions of pollutants in the region. Monitoring the presence of atmospheric pollutants, as well as studying their transport and dispersion is important in this polluted area, and continuous monitoring of the development of the PBL in the region can be useful to obtain information regarding local air quality. Air pollution in the area mostly originates from fossil fuel consumption. The city has a vehicular fleet of over 7 million (CARVALHO et al., 2015), and vehicular traffic is the main source of pollutant emissions in the city. Biomass burning from

nearby regions also contribute to air pollution in the city. The city is located in the southeast of Brazil and has a humid subtropical climate (Cwa). Summers (January-March) in the city are warm and wet, and winters (July-September) are dry and mild.

Lidar and ceilometer data were obtained at the IPEN and CIENTEC sites, respectively. CO_2 data was obtained from Picarro CRDS spectrometers located in three different experimental sites in the city: IAG, UNICID and Pico do Jaraguá. Experimental site locations and approximate distance between them are shown in figures 12 and 13.

Experimental site locations:

- IPEN (23°34’ S, 46°3 W): located in a suburban setting, approximately 782 m above sea level. The lidar is located at the Center for Lasers and Applications of the Nuclear and Energy Research Institute building.
- CIENTEC (23°39’ S, 46°37’ W): a CHM15k ceilometer located on the rooftop of the Museum of Meteorology of the Science and Technology Park (CIENTEC) of the University of São Paulo. The site is located in a suburban setting, approximately 810 m above sea level.
- IAG (23°33’ S, 46°44’ W): is located in a suburban setting, approximately 731 m above sea level. The inlet sits at the rooftop of the Institute of Astronomy, Geophysics and Atmospheric Sciences (IAG) of the University of São Paulo, 15 m above ground level. An urban highway is located approximately 1 km from the site, with an average daily traffic of over 250000 vehicles (CET-SP, 2021).
- UNICID (23°32’ S, 46°33’ W): located in an urban setting, approximately 741 m above sea level. The inlet is located at the rooftop of the City University of São Paulo (UNICID), at 38 m above ground level. A busy road is located only a few meters from the site, as well as an over ground metro line. A sewage treatment station is located approximately 2.5 km from the site.
- Pico do Jaraguá (23°27’ S, 46°45’ W) is located in the Pico do Jaraguá (Jaraguá Peak), one of the highest places in the city, and is surrounded by the Jaraguá forest reserve. The site elevation is 1079 m, and the inlet is located 3 m above ground level.

Figure 12: Location of IPEN and CIENTEC stations.

Source: Google Maps, 2023.

Figure 13: Locations of IAG, UNICID and Pico do Jaraguá stations.

Source: Google Maps, 2023.

4.2 Instrumentation

4.2.1 MSP-LIDAR I

The lidar system used in this work is the MSP-LIDAR I (MSP-I), located at the IPEN Center for Lasers and Applications. The instrument uses a Nd:YAG laser commercialized by Quantel, model Brilliant B. The laser operates at a fundamental wavelength of 1064 nm, generating second and third harmonics at 532 nm and 355 nm, and with a repetition rate of 10 Hz. The beam diameter is 9 mm, and the beam duration is 6 ± 2 ns. The telescope has a 30 cm mirror with a focal length of 1.5 m, and the system has a field-of-view of 0.1 mrad. More information can be found on the laboratory's website at http://gescon.ipen.br/leal/4.Equipments.html.

Figure 14 shows the MSP-LIDAR I at its operating location.

Figure 14: MSP-LIDAR I operating at the Center for Lasers and Applications – IPEN.

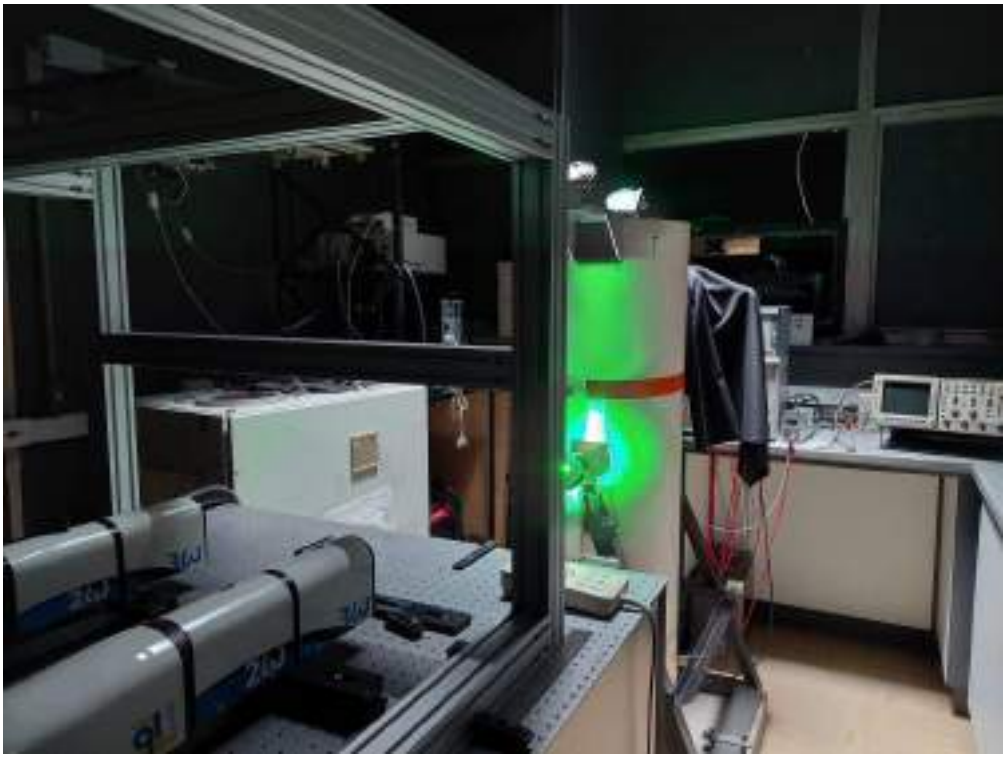

Source: author, 2023.

4.2.2 Lufft CHM 15k Ceilometer

The ceilometer used in this work, shown in Figure 15, is the CHM 15k, commercialized by Lufft, located at Parque CIENTEC.

Figura 15: CHM 15k ceilometer at CIENTEC.

Source: author, 2023.

The instrument has an eye-safe system equipped with a solid-state Nd:YAG laser that operates at a single infrared wavelength at 1064 nm. It has a range of 15 km, with a vertical resolution of 5 m for measurements and 15 m in the NetCDF file. Its temporal resolution is fixed at 15 s. The laser pulse has a duration of 1 to 5 ns, with a repetition rate of 5 – 7 kHz and energy of 8 µJ. The beam diameter is expanded up to 90 mm, with a divergence of less than 0.3 mrad. The receiver's field-of-view is 0.45 mrad. More information can be found in the instrument manual (https://www.lufft.com/download/manual-lufft-chm15k-en/).

4.2.4 Picarro CRDS gas analyzer

The analyser used to measure the ambient air concentrations of CO_2 was the Picarro Cavity Ring-Down spectrometer (Picarro Inc., USA) G2301 at IAG and Pico do Jaraguá station and G2401 at UNICID station. This instrument is a high-precision GHG analyzer. It makes simultaneous measurements of CH_4 and CO_2 at parts-per-billion (ppb) and water (H_2O) at parts-per-million (ppm) with extremely low drift. This

instrument meets the performance requirements for CO_2 and CH_4 monitoring defined by the World Meteorological Organization (WMO) and Integrated Observation System (ICOS). The concentrations are measured by the instrument using Cavity Ring-Down Spectroscopy (CRDS) technique.

G2301 model:

For CO_2 measurements, precision is < 70 ppb at 5 seconds and < 25 ppb at 5 minutes. For CH_4 measurements, precision at 5 seconds and 5 minutes are < 0.5 and < 0.22 ppb respectively. At standard temperature and pressure (STP), the maximum drift of the measurement data is < 120 ppb for CO_2 and < 1 ppb for CH_4 over 24 hours. More about the instrument can be read on the manufacturer's website (https://www.picarro.com/g2301_gas_concentration_analyzer).

G2401 model:

For CO_2 measurements, precision is 50 ppb at 5 seconds and 20 ppb at 5 minutes. For CH_4 measurements, precision at 5 seconds and 5 minutes are 1 and < 0.5 ppb, respectively. At standard temperature and pressure (STP), the maximum drift of the measurement data is 100 ppb for CO_2 and 1 ppb for CH_4 over 24 hours. More about the instrument can be read on the manufacturer's website (https://www.picarro.com/g2401_gas_concentration_analyzer).

5 RESULTS AND DISCUSSION

5.1 Case studies

Three case studies will be presented: section 5.1.1 – well-defined PBL; section 5.1.2 - presence of clouds, and section 5.1.3 - presence of aerosol layers. PBLHs values retrieved from lidar data will be referred as $PBLH_{lidar}$, and from ceilometer data, as $PBLH_{ceil}$.

5.1.1 Well-defined PBL

Data from May 19th, 2021, was selected to compare the results obtained by the instruments in a clear-sky day and the PBL is well-defined. The Lidar MSP-I system operated on this day from 12:08 to 22:35 UTC, and this will be the interval considered in the comparison. Figure 16 shows the evolution of the RCS obtained with the MSP-I data throughout the day, as well as the PBLHs obtained by the WCT method with the instrument data. Figure 17 shows the RCS of the CHM 15k in the same range, as well as the PBLH values calculated with the data from this instrument.

Figure 16 – RCS measured by the MSP-I lidar as a function of height and time of day (UTC) on May 19th, 2021. PBLHs obtained from the lidar data are shown in black.

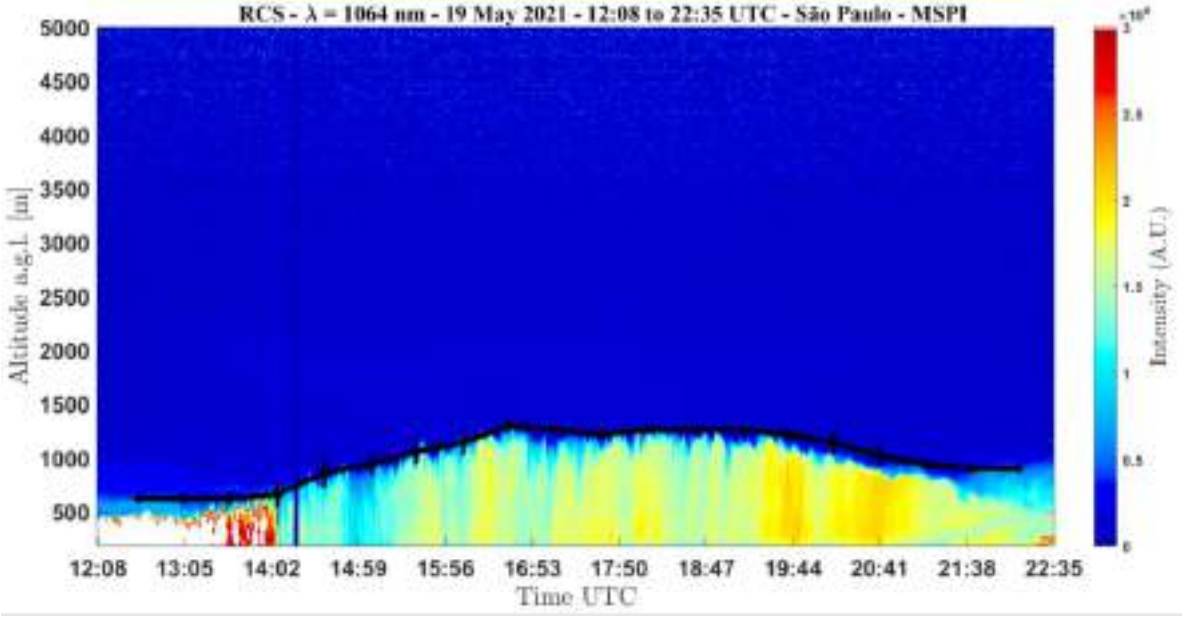

Source: author, 2023.

Figure 17 – The same as the previous figure, but for CHM 15k ceilometer data on May 19th, 2021.

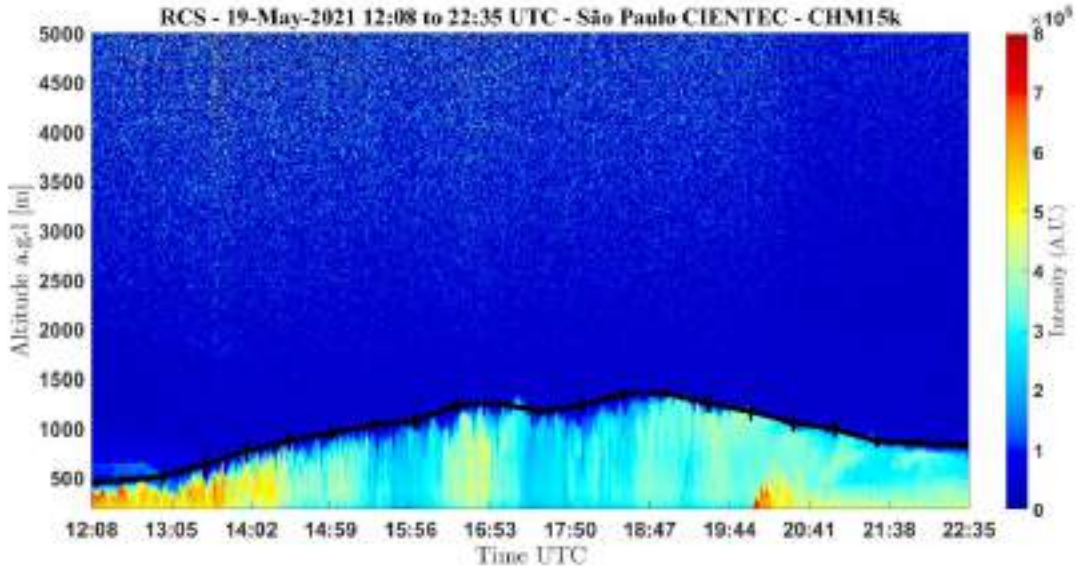

Source: author, 2023.

During the interval considered in this case, we see the PBL has a typical presentation for clear-sky days, growing from mid-morning to early afternoon, the PBL top reaches its peak height in mid-afternoon, and PBL collapse starts in mid-to-late afternoon.

Figure 18 shows the variation between the values found for $PBLH_{lidar}$ in relation to the results obtained for $PBLH_{ceil}$.

Figure 18 – Difference between $PBLH_{lidar}$ and $PBLH_{ceil}$ values obtained on May 19th, 2021.

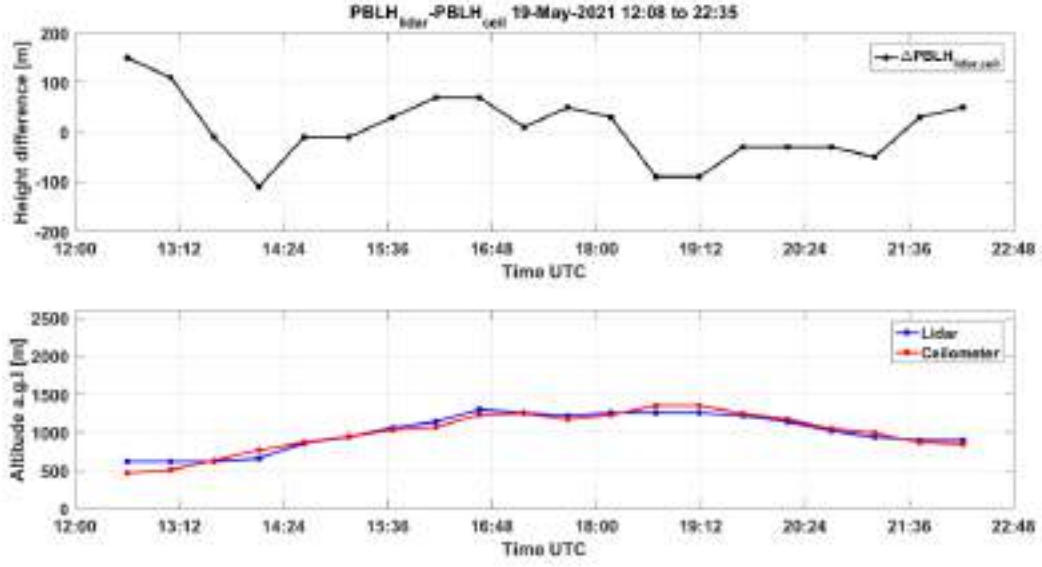

Source: author, 2023.

At around 17:00 local time (20:00 UTC), data from both instruments show the development of a lower layer closer to the ground. This corresponds to the arrival of maritime breezes, commonly detected in late-afternoon. Sea breeze is one of the thermally driven circulations affecting local weather patterns in the Metropolitan Region of São Paulo (MRSP), and sea breeze fronts disrupt convective growth of the boundary layer (RIBEIRO et al., 2018; OLIVEIRA et al., 2003). The presence of this layer attenuates the signal, making it more difficult to see the PBLH above it. It can also be difficult to identify the CBL due to the developing Residual Layer. As we can see in Figure 16, the PBL top is still visible, but could be mistaken for the Residual Layer above it. This difference is even more difficult to see in the ceilometer signal, making it hard to separately identify the maritime breeze, the CBL and the RL.

Despite not being co-located, the PBLH values obtained with both instruments do not show great variation. From Figures 16 and 17, we can estimate Convective Boundary Layer growth starting in late-morning, around 10:00 local time (13:00 UTC). The PBLH values obtained with the WCT method start decreasing at around 16h30 local time (19h30 UTC). Data from both instruments show similar diurnal evolution in both locations.

This case study shows that, in clear-sky days when the PBL is well defined, the results of the two instruments present good agreement with each other.

5.1.2 Cloudy conditions

To illustrate a situation where there is the presence of clouds at heights close to the PBLH, data from June 16th, 2021, was selected to compare the results obtained by the instruments. The MSP-I Lidar operated on this day from 13:25 until 21:28 UTC, this being the time interval considered in the comparison. Figure 19 shows the evolution of the RCS obtained with the MSP-I data in the period, as well as the PBLH values calculated by the WCT method with the instrument data ($PBLH_{lidar}$). Figure 20 shows the RCS of the CHM 15k in the same range, as well as the PBLH values calculated with the data from this instrument ($PBLH_{ceil}$).

Figure 19 – RCS measured by the MSP-I lidar as a function of height and time of day (UTC) on June 16th, 2021. PBLHs obtained from the lidar data are shown in black.

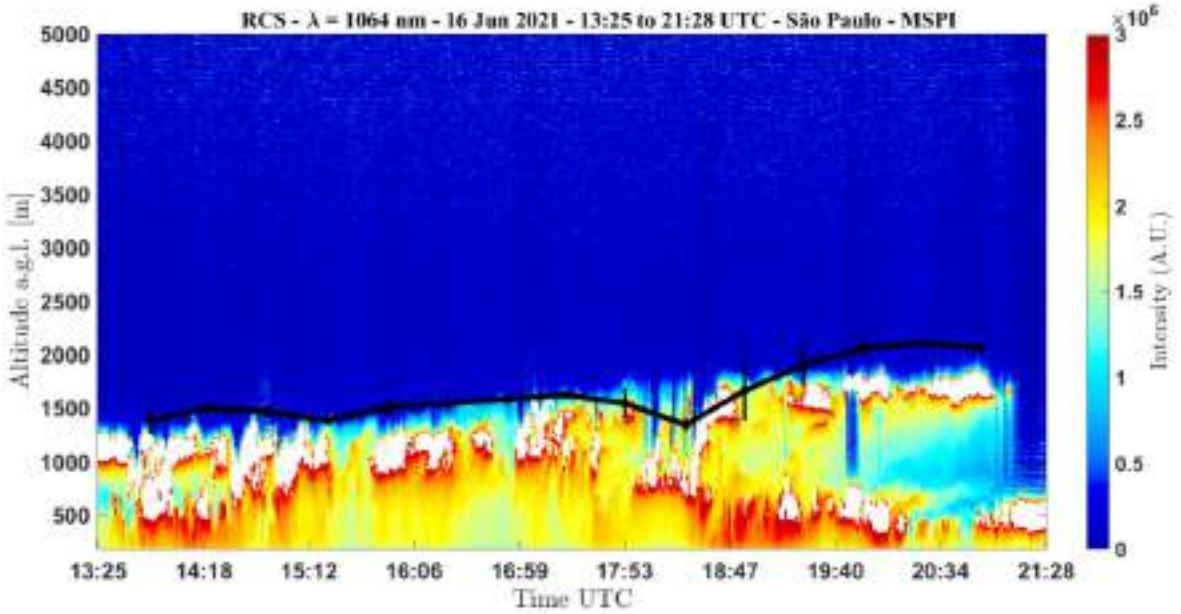

Source: author, 2023.

Figure 20 – The same as the previous figure, but for CHM 15k ceilometer data on June 16th, 2021.

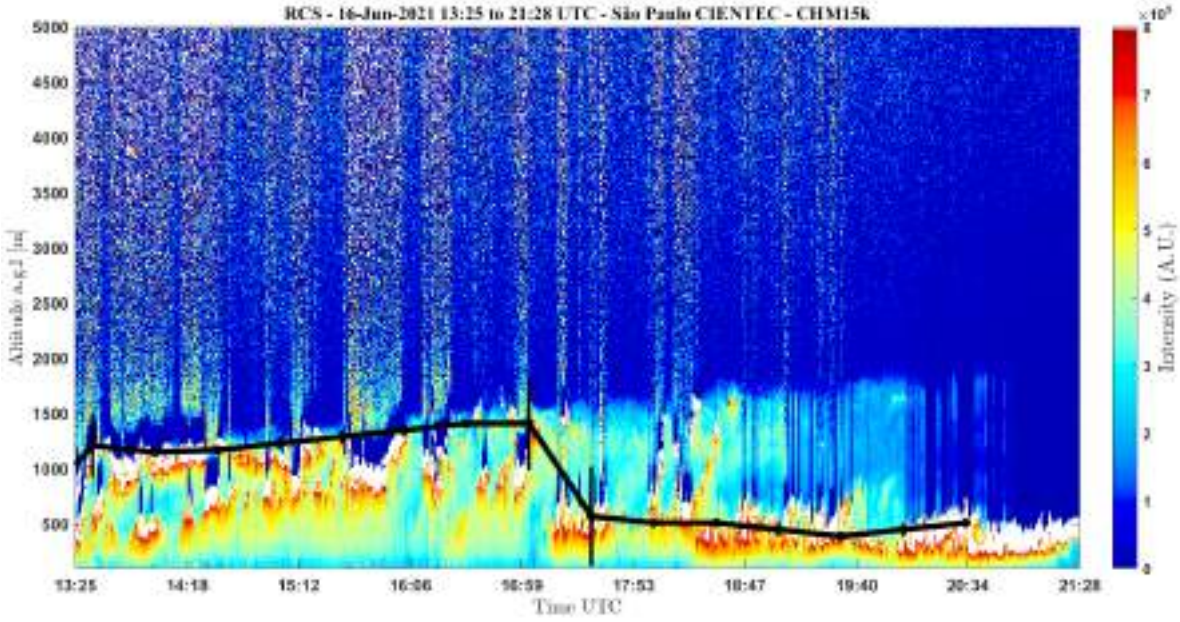

Source: author, 2023.

From figures 19 and 20, signal of both instruments is attenuated, but it is still possible to estimate the boundary layer top in some of the profiles. For profiles obtained with the ceilometer, signal attenuation is significant. As the WCT method identifies abrupt changes in aerosol concentration, it is not possible to confirm if the obtained PBLH is accurate when there is significant signal attenuation.

Figure 21 shows the $\Delta PBLH_{lidar\text{-}ceil}$ difference calculated every 30 minutes in the considered interval.

Figure 21 – Difference between $PBLH_{lidar}$ and $PBLH_{ceil}$ values obtained on June 16th, 2021.

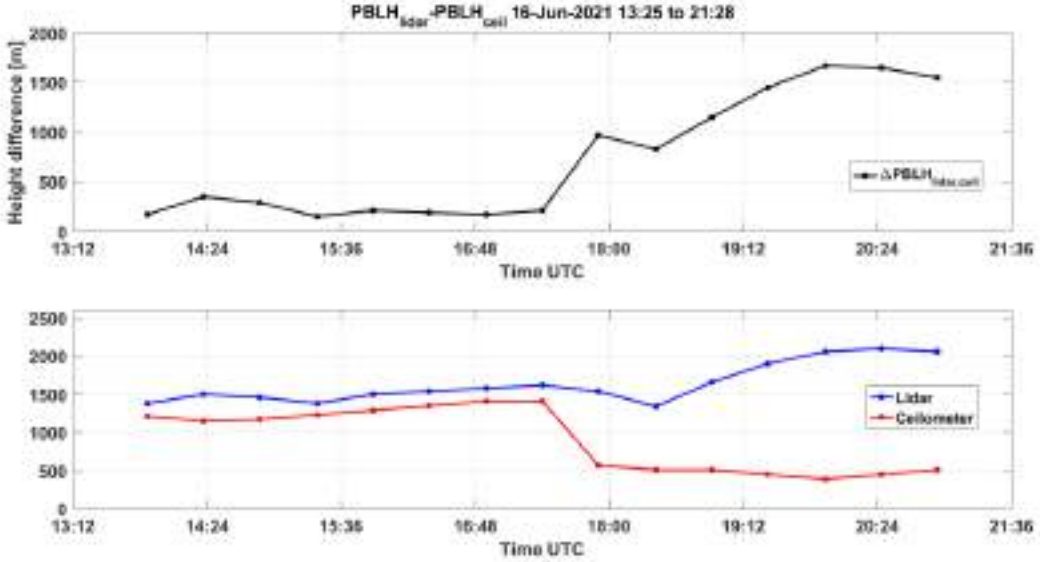

Source: author, 2023.

The presence of low clouds resulted in a greater divergence between the results from both instruments when compared to the first case study. This highlights the different instrument capabilities, as well as the variability in the spatial and temporal distribution of clouds between the two locations.

5.1.3 Aerosol layers

The third case study corresponds to a situation where there is the presence of aerosol layers near the top of the PBL. Data from September 14th, 2021 was selected. The MSP-I Lidar operated on this day from 13:03 to 19:25 UTC. For comparison purposes, the same interval was selected for the CHM 15k ceilometer data. Figure 22 shows the evolution of the MSP-I RCS in this selected time period, as well as the calculated $PBLH_{lidar}$ values. Figure 23 shows the same, but for RCS and $PBLH_{ceil}$ of the ceilometer.

Figure 22 – RCS measured by the MSP-I lidar as a function of height and time of day (UTC) on September 14th, 2021. PBLHs obtained from the lidar data are shown in black.

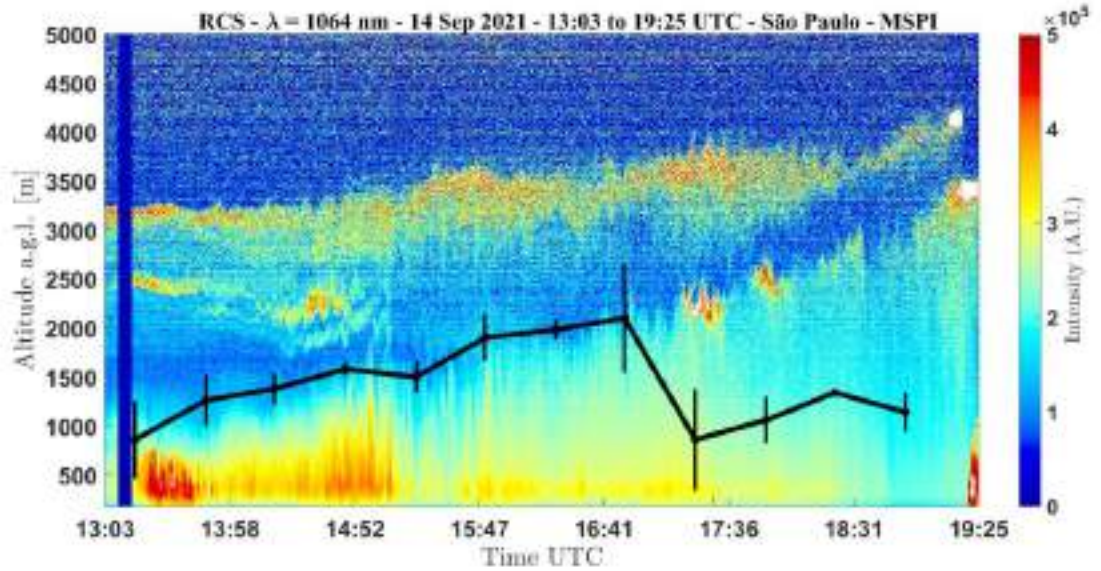

Source: author, 2023.

Figure 23 – The same as the previous figure, but for CHM 15k ceilometer data on Sempteber 19th, 2021.

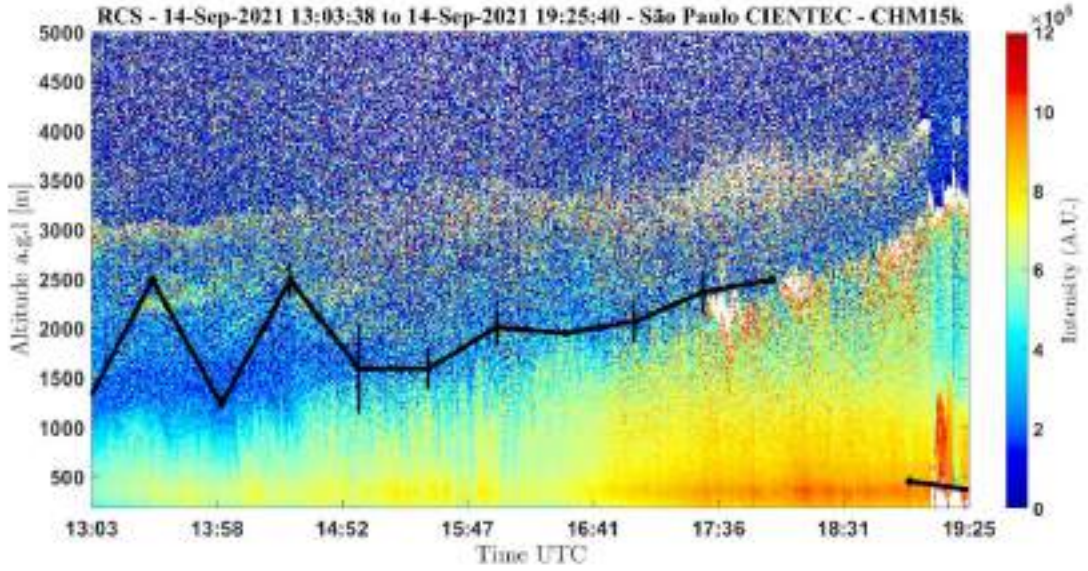

Source: author, 2023.

In figures 22 and 23, it is possible to observe the presence of aerosol layers below 3.5 km with the data from the two instruments. As the PBLH increases throughout the day, the top of the Boundary Layer grows closer to the aerosol layer above it. We see that the presence of these layers caused variations in the calculated PBLH values. For $PBLH_{ceil}$, the top layer was considered as the PBLH by the WCT method twice.

Figures 22 and 23 appear to show the top layer of aerosols at different heights at the two locations. A $\Delta PBLH_{lidar\text{-}ceil}$ difference of a few meters was therefore expected. Figure 24 shows the variation between the values found for $PBLH_{lidar}$ in relation to the results obtained for $PBLH_{ceil}$ in the chosen time-interval. $PBLH_{ceil}$ values remained higher than $PBLH_{lidar}$ for almost the entire time-interval shown.

Figure 24 – Difference between $PBLH_{lidar}$ and $PBLH_{ceil}$ values obtained on September 14th, 2021.

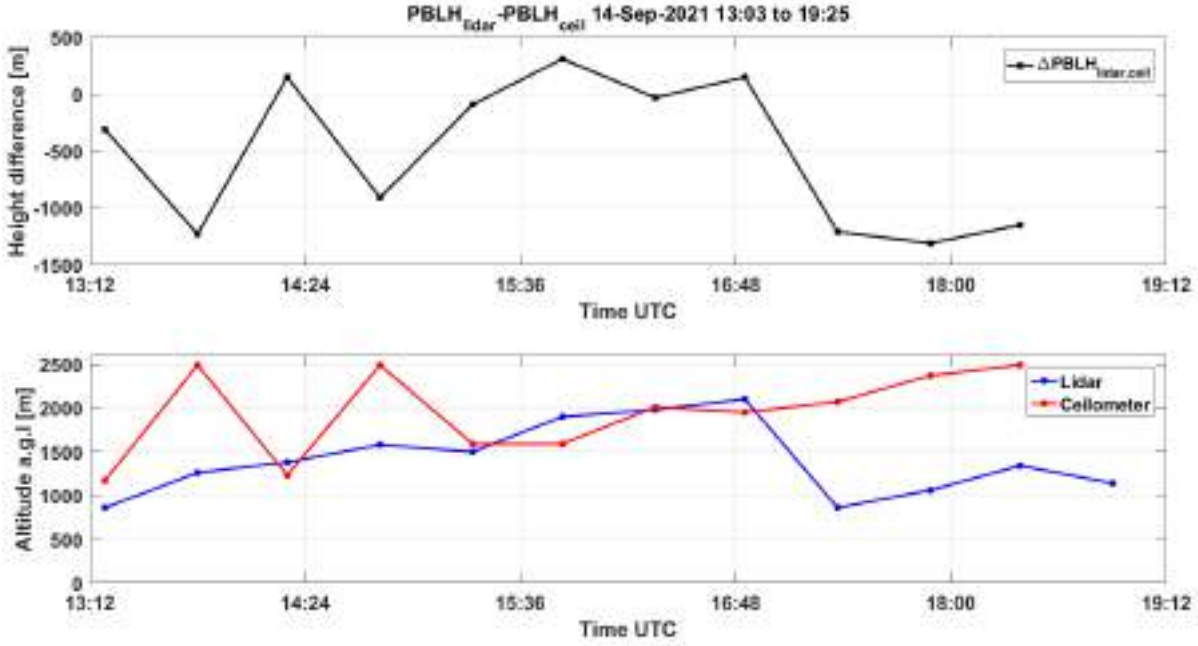

Source: author, 2023.

5.2 Chosing the dilation '*a*' and the threshold values

In order to obtain accurate results for PBLHs retrieved through the WCT method, adequate values must be chosen for the parameter *a*.

Figure 25 shows the RCS measured by the CHM 15k ceilometer on July 15th, 2021, and the PBLHs retrieved when using different values of *a.*

Figure 25: RCS measured by the CHM 15k ceilometer as a function of height and time of day (UTC) on July 15th, 2021 and PBLHs obtained from the ceilometer data for different values of *a*.

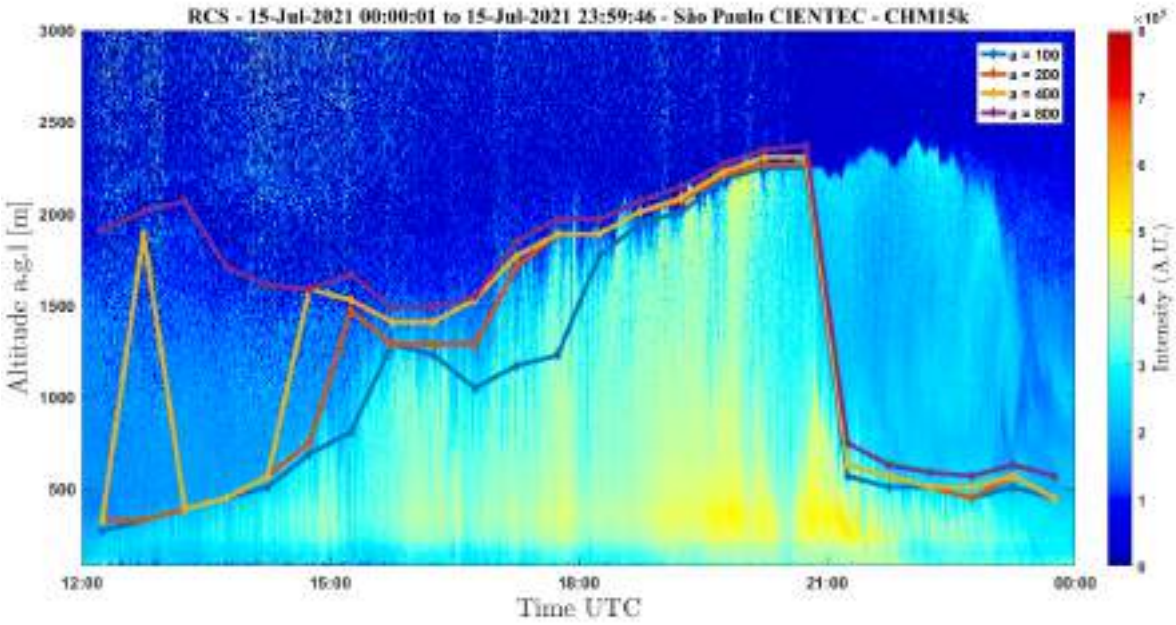

Source: author, 2023.

From figure 25, we see that the choice of the parameter *a* was determinant in finding the PBLH. From 12:00 to 15:00 UTC, the Residual Layer was still evident in the profiles and, when using higher values for *a*, the RL was detected instead of the developing ML. On the other hand, too low values of *a* can cause the detection of PBLH values that are lower than the real values, as seen in figure 25 from 17:00 to 18:00 UTC.

For PBLHs obtained from CHM 15k data presented in this work, the dilation was defined as *a* = 200.

The maximum value of the WCT function does not always correspond to the PBL top height. Aerosol layers within the boundary layer can sometimes be misidentified as the PBLH. Choosing a threshold condition can improve the accuracy of the results, by searching for a value of *W(a,b)* that is a certain percentage smaller than the maximum of the function. While choosing a threshold condition can be helpful in some situations, in the presence of aerosol layers above the PBL it can cause the misidentification of the aerosol layer as the PBLH.

PBLHs obtained on September 27, 2021 when using different threshold values are shown in figure 26.

Figure 26: RCS measured by the CHM 15k ceilometer as a function of height and time of day (UTC) on September 27th, 2021. PBLHs obtained from the ceilometer data using different threshold values are shown in blue, red, yellow, purple and green (threshold = 0.75, 0.80, 0.85, 0.90, 0.95).

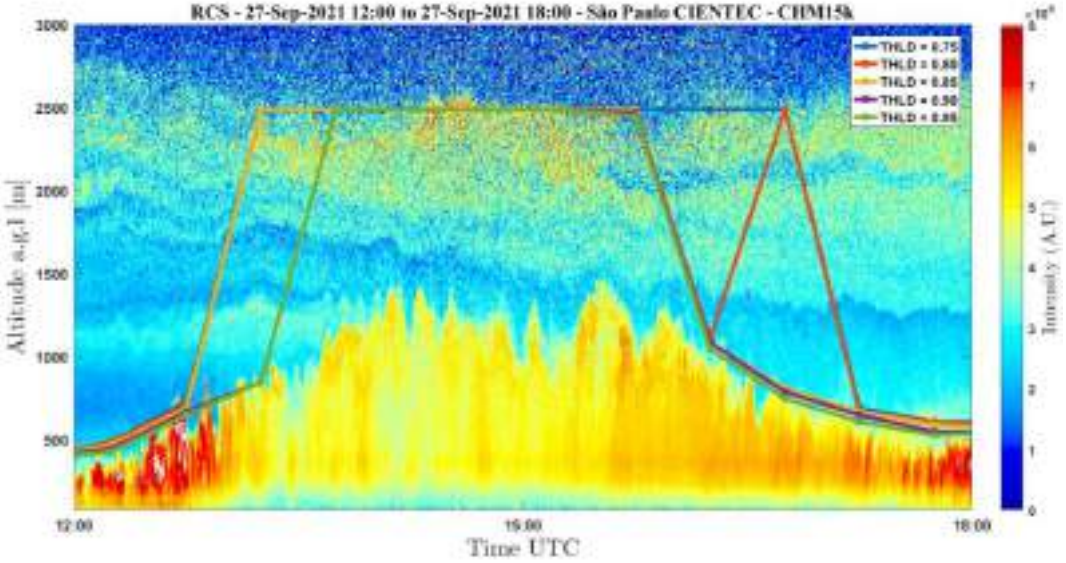

Source: author, 2023.

The high backscattering signal from the aerosol layer at 2000-2500 m caused the overestimation of the PBL height. Using lower threshold values caused this to happen to a greater number of profiles. In figure 27, the 30 minute average of the RCS between 16:00:05 and 16:30:04 UTC is shown, as well as the WCT values obtained in the same period when using different threshold conditions.

Figure 27 - RCS and WCT profile obtained on September 27th, 2021 from 30-minute average data between 16:00:05 and 16:30:04 UTC and the maximum values of *W(a,b)* obtained using different threshold values.

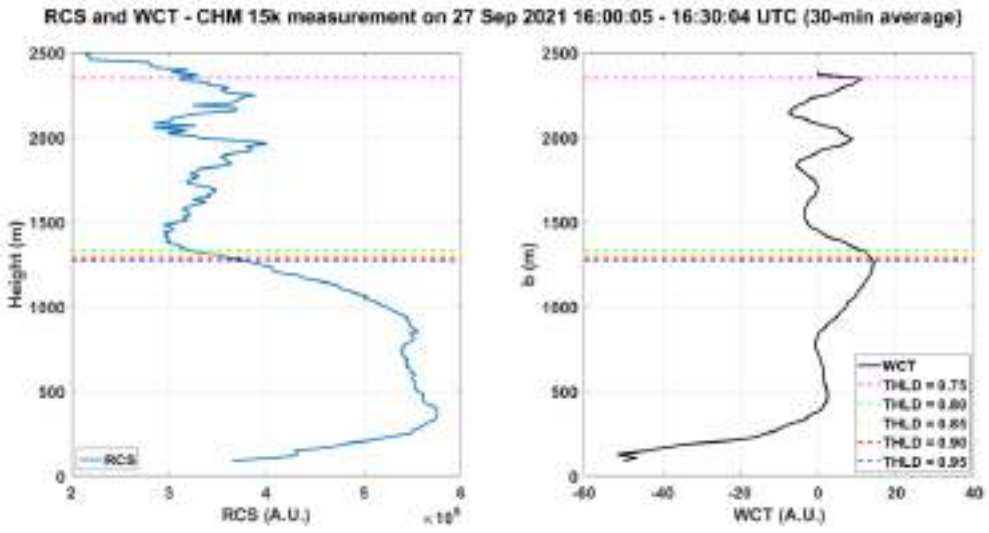

Source: author, 2023.

From figure 28, we see that using threshold values above 0.80 resulted in good PBLH estimates, but with a threshold of 0.75 the aerosol layer was identified as the PBLH instead. We can also see from figure 28 that with lower threshold conditions can the method is less likely to underestimate the PBL height.

A threshold value of 0.80 was used for the PBLHs obtained from CHM 15k ceilometer data in this work.

5.3 The PBLH cycle

The CHM 15k ceilometer operated daily from February to December 2021. Data from the instrument include automatic estimates of cloud base heights for each profile. Even though these estimates are not always accurate, this information is useful for filtering the data. As seen in case study 2, the presence of low clouds close to the top of the PBL can impair the retrieval of PBLH values.

From this point forward, $PBLH_{ceil}$ will be referred to as simply PBLH.

5.3.1 Diurnal PBLH cycle

CHM 15k ceilometer data from February 3 to December 31, 2021 was used to calculate the PBLH in this interval. Profiles where the instrument detected clouds below 2.5 km were removed from the analysis. Figure 28 shows the average values of $PBLH_{ceil}$ obtained throughout the day, with a time average of 30 minutes. The errorbars correspond to the standard deviation of all profiles included in the average.

Figure 28 – Average of the PBLH values obtained from February 3rd to December 31st, 2021.

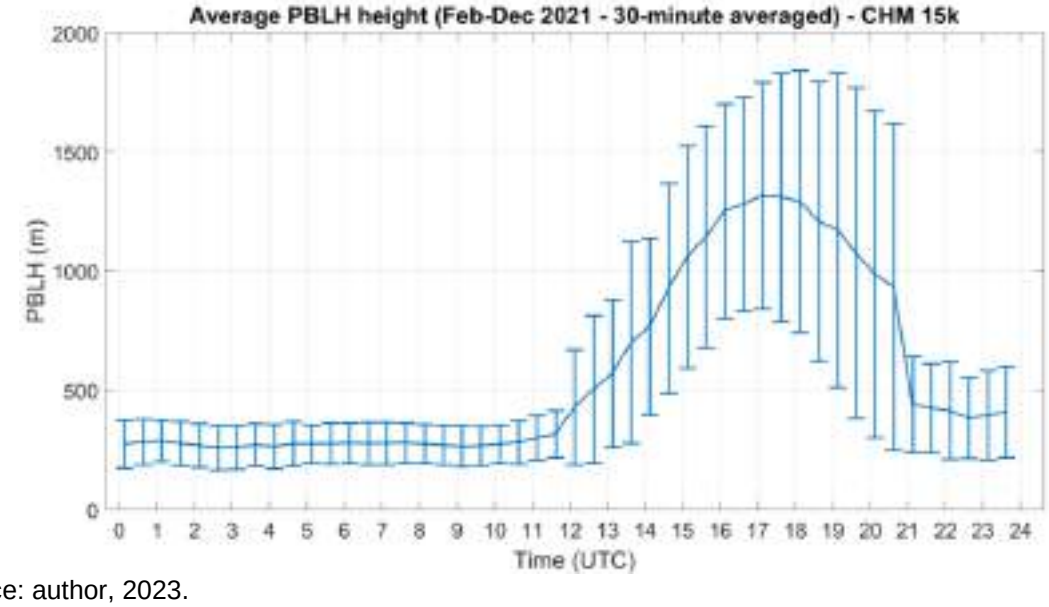

Source: author, 2023.

As seen in figure 28, the highest mean value of $PBLH_{ceil}$ was observed at 17:00-17:30 UTC. It is possible to see a PBLH diurnal growth pattern which corresponds to what is expected for the diurnal cycle of the PBL, with its top height increasing during the morning, reaching its maximum value in early-to-mid afternoon.

5.3.2 Seasonal PBLH cycle

Mean PBLH values were calculated for each month in the measurement range, and these values are shown in Figure 29. The errorbars correspond to the standard deviation of all profiles included in the average.

Figure 29 – Monthly average PBLH obtained from February to December 2021.

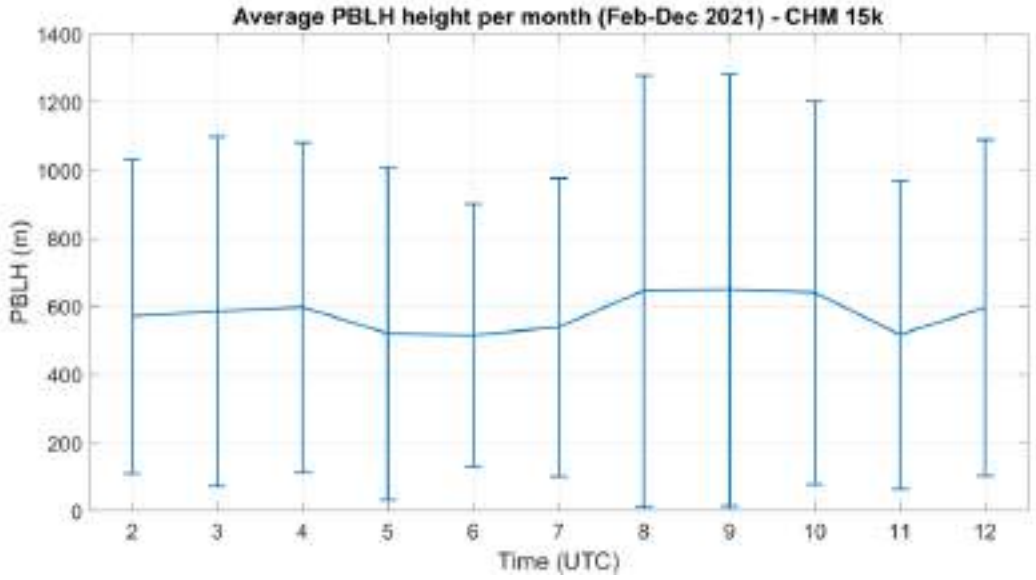

Source: author, 2023.

From figure 29, it is possible to observe that throughout the analyzed period the PBLH average value per month remained between 400 and 800 m. However, the values vary widely, as can be seen by the error bars included in the figure.

5.4 Application of results: PBLH and CO_2 concentration comparisons

PBLH values obtained with the CHM 15k data were compared to CO_2 concentration data from three experimental sites. The CO_2 concentration profiles were 30-minute averaged, as well as the ceilometer data. The number of valid data points from each location are shown in table 1. Table 2 shows the number of valid data-points for each CO2 measurement location that have equivalent valid CIENTEC data-points.

Table 1: Number of valid PBLH (CIENTEC) and CO_2 data-points.

Data points	CIENTEC (PBLH)	IAG (CO2)	UNICID (CO2)	Jaraguá (CO2)
Feb	512	1289	1342	0
Mar	805	1488	1136	828
Apr	549	1440	1278	1428
May	672	952	790	1360
Jun	539	1269	1388	1145
Jul	932	1488	1345	1480
Aug	542	1488	1319	1451
Sep	286	1440	1372	1399
Oct	256	1488	1480	505
Nov	338	1440	1264	1260
Dec	209	1448	244	1476
Total	5640	15270	12958	12332

Table 2: Number of valid CIENTEC data-points and number of data-points at IAG, UNICID, and Pico do Jaraguá that have equivalent valid CIENTEC data-points.

Data points	CIENTEC (PBLH)	IAG (CO2)	UNICID (CO2)	Jaraguá (CO2)
Feb	512	508	511	0
Mar	805	805	534	528
Apr	549	549	414	545
May	672	616	310	670
Jun	539	488	506	398
Jul	932	932	878	926
Aug	542	542	542	538
Sep	286	286	246	257
Oct	256	256	256	62
Nov	338	338	314	338
Dec	209	209	0	209
Total	5640	5529	4511	4471

5.4.1 Monthly average PBLH and CO2

The monthly average PBLH and CO2 concentrations are show in figures 30 to 33.

Figure 30 – Monthly average PBLH obtained from February to December 2021 with fitted curve.

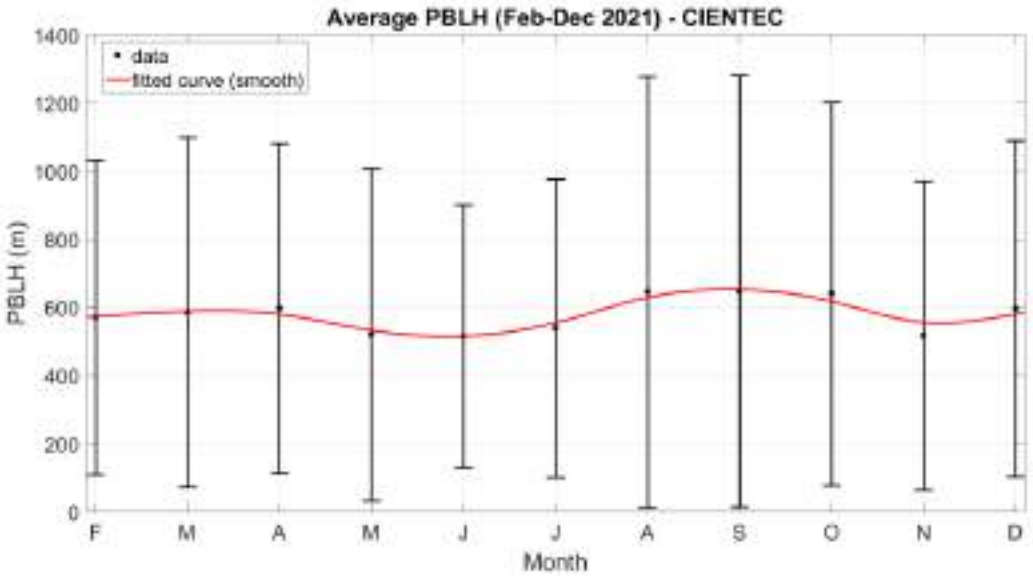

Source: author, 2023.

Figure 31 – Monthly average CO_2 concentrations obtained from February to December 2021 at IAG.

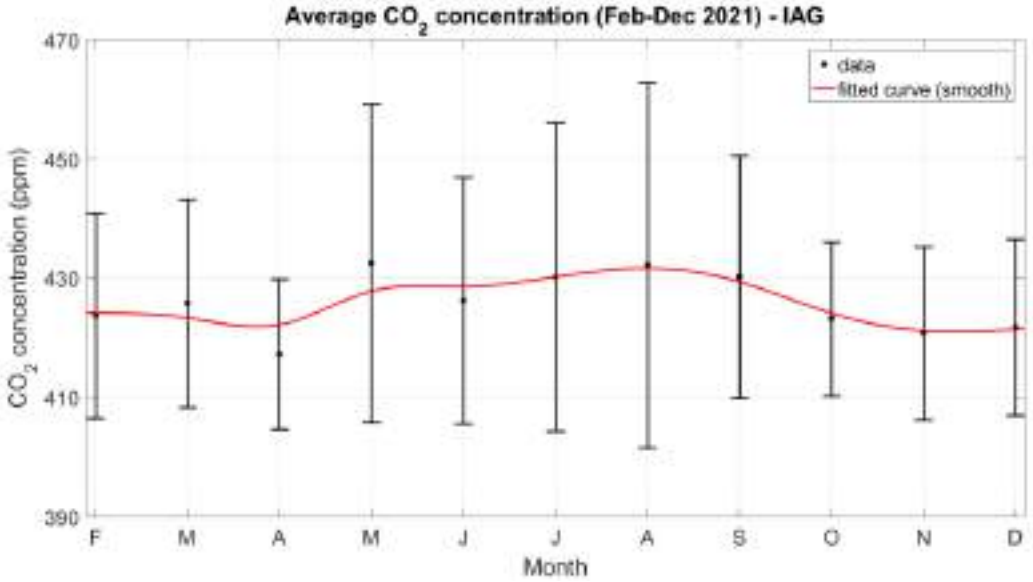

Source: author, 2023.

Figure 32 – Monthly average CO_2 concentrations obtained from February to December 2021 at UNICID.

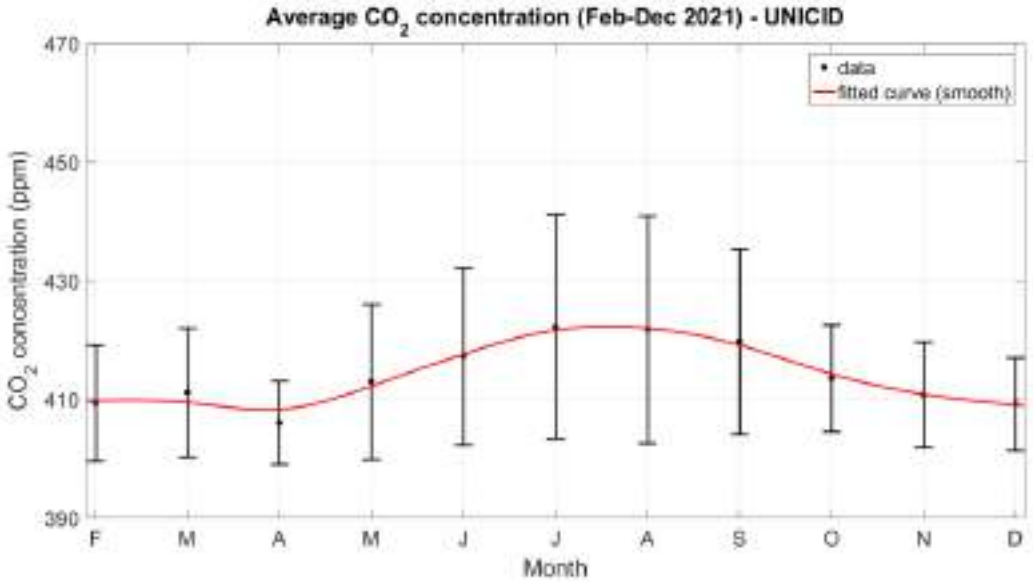

Source: author, 2023.

Figure 33 – Monthly average CO_2 concentrations obtained from February to December 2021 at Pico do Jaraguá.

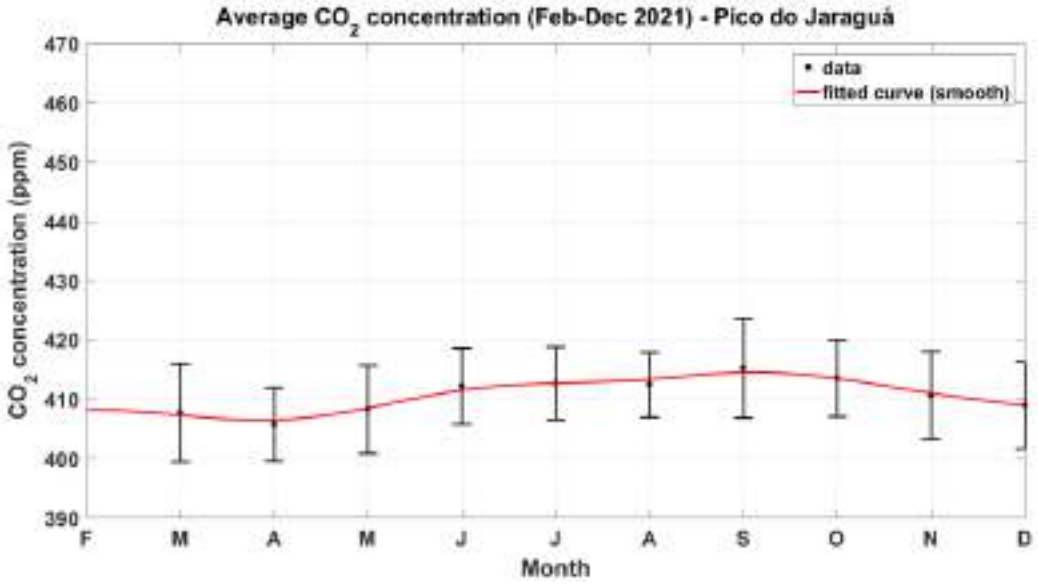

Source: author, 2023.

The highest average CO2 concentrations were measured during or around the winter months (June-September). In all stations, the lowest CO2 concentrations were measured in April. The monthly average PBLH shows more variability, not

exhibiting a clear pattern. During the winter months, São Paulo experiences its dry season and the temperature fluctuates between cold, mild and warm. During summer and spring, rainfall is common and obtaining the PBLH is not always possible due to the rain and cloudy conditions. These variations can make it hard to see the actual changes the PBL presents throughout the year, and the monthly average includes nighttime PBLHs, which vary only a few hundred meters from day to day. The PBL seasonal cycle becomes more evident when analyzing the average PBLH for different times of the day. The average monthly PBLH at 10:00, 12:00, 14:00 and 16:00 UTC were obtained and are shown in figure 34. Figures 36-38 show the average CO_2 concentrations at the three experimental sites.

Figure 34 – Monthly average PBLH values obtained from February to December 2021 at 10:00, 12:00, 14:00 and 16:00 UTC.

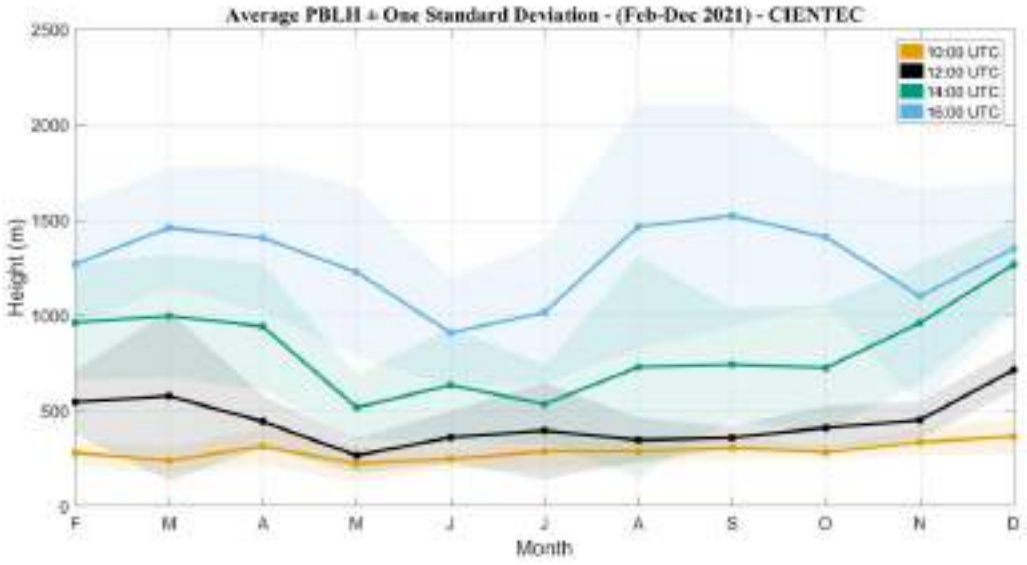

Source: author, 2023.

Figure 35 – Monthly average CO_2 concentrations obtained at IAG from February to December 2021 at 10:00, 12:00, 14:00 and 16:00 UTC.

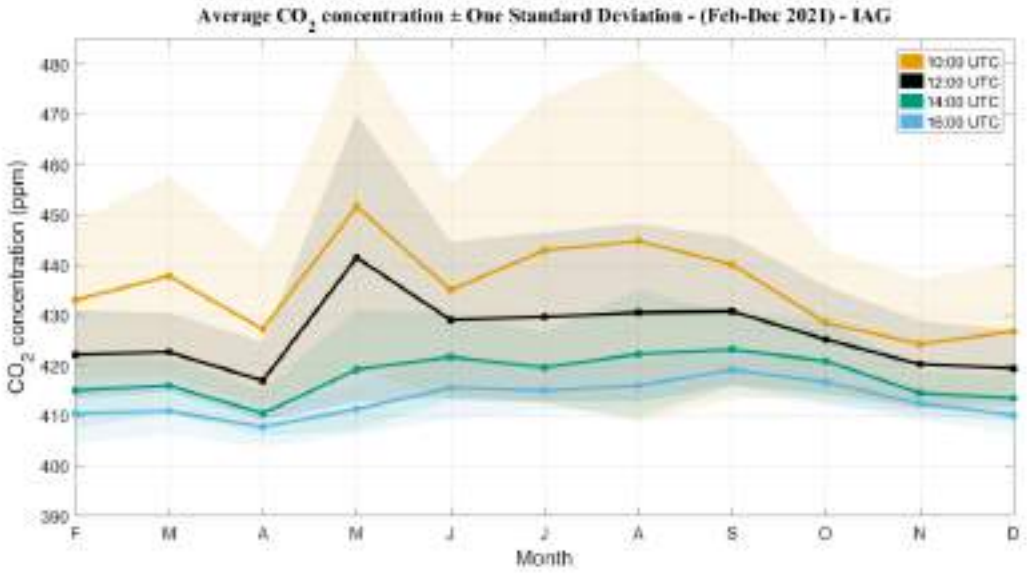

Source: author, 2023.

Figure 36 – Monthly average CO_2 concentrations obtained at UNICID from February to December 2021 at 10:00, 12:00, 14:00 and 16:00 UTC.

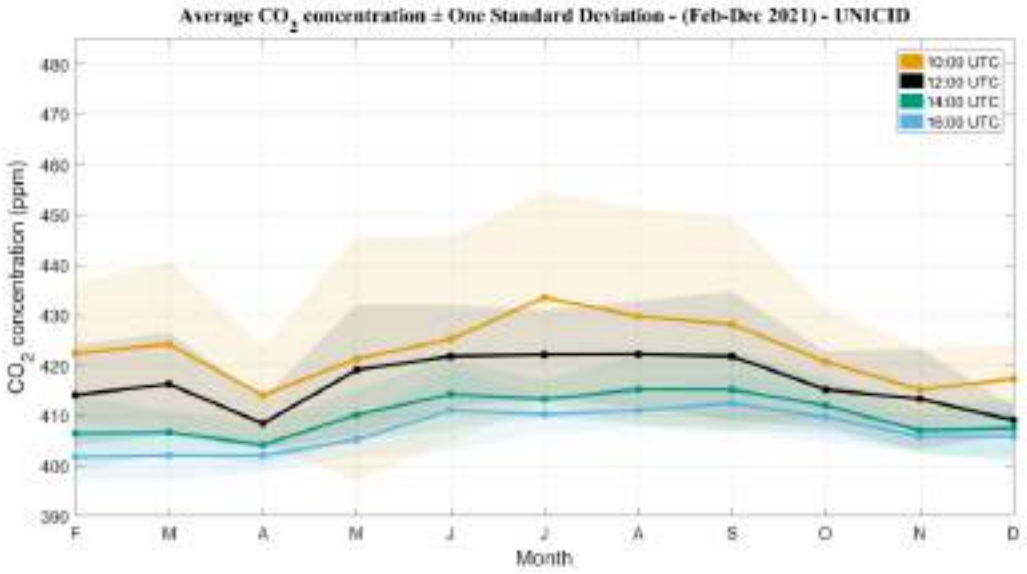

Source: author, 2023.

Figure 37 – Monthly average CO_2 concentrations obtained at Pico do Jaraguá from February to December 2021 at 10:00, 12:00, 14:00 and 16:00 UTC.

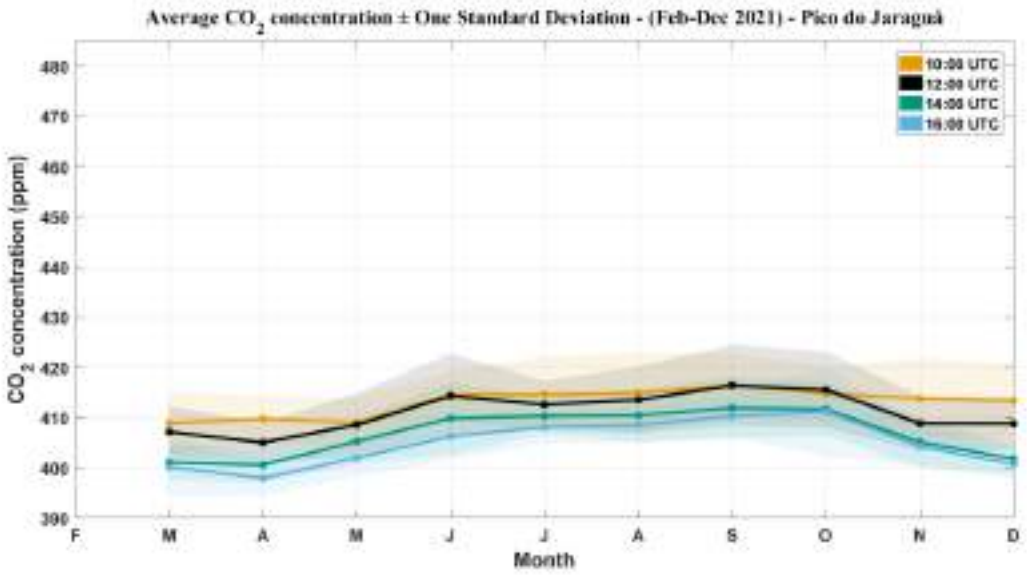

Source: author, 2023.

In figure 34, we can see a clear pattern of PBLH growth during morning and early afternoon. Early morning heights at 10:00 UTC are still similar to nocturnal boundary layer heights, and, during most days, the PBL top is already nearing its maximum height by 16:00 UTC. A decrease in PBLHs is seen in during the colder months and this is mostly consistent throughout the day, with colder months having lower PBLHs during daytime and nighttime. PBLHs obtained at 16:00 UTC show more variability than those obtained for earlier in the day.

In figures 35-37, the average CO2 concentrations are shown to increase during the winter months. CO2 concentrations show more variability earlier in the day. This increase in CO2 concentrations during the colder months and decrease during the warmer months is seen throughout the day, with colder months showing higher CO2 concentrations during daytime and nighttime. At UNICID and Pico do Jaraguá, there was a decrease in CO2 concentrations from March to April, in sharp constrast to the slightly increasing concentrations seen between February and March.

Average PBLHs and CO2 concentrations show negative correlation, with PBLH values significantly decreasing from April to May, at the same time that a sharp rise in CO2 concentrations is seen. Peak CO2 concentrations vary from station to

station, with IAG having its peak in May, UNICID in July, and Pico do Jaraguá in September.

Rainfall is more common in São Paulo during the afternoon and night than earlier in the day, therefore morning to late afternoon is a favorable time for accurate PBLH detection. Between late morning and early afternoon, due to increasing incident solar radiation, the PBL quickly expands. The average PBLH at noon varies throughout the year. In figure 38-41, average PBLHs and CO2 concentrations at 12:00 local time are shown. Each data point corresponds to a 30-minute average measurement at 15:00 UTC from February to December 2021.

Figure 38 – All PBLH values obtained at 15:00 UTC (12:00 local time) from February to December, 2021 at CIENTEC.

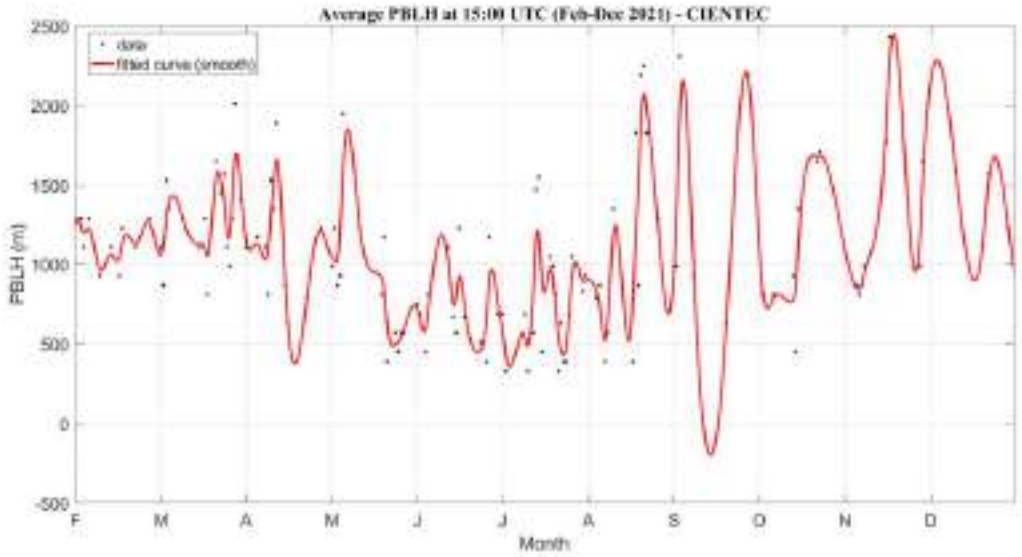

Source: author, 2023.

Figure 39 - All CO_2 concentrations obtained at 15:00 UTC (12:00 local time) from February to December, 2021 at IAG.

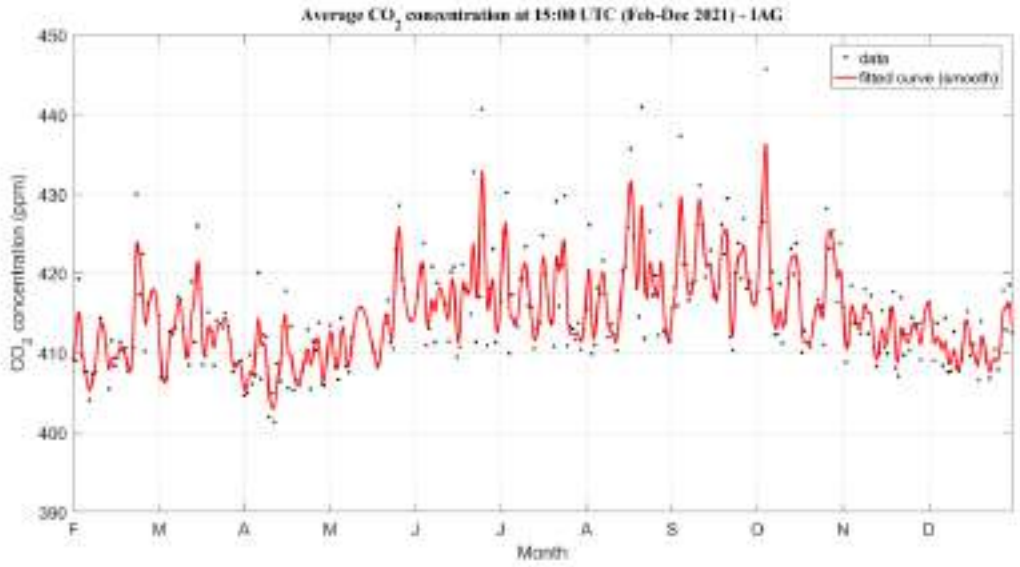

Source: author, 2023.

Figure 40 - All CO_2 concentrations obtained at 15:00 UTC (12:00 local time) from February to December, 2021 at UNICID.

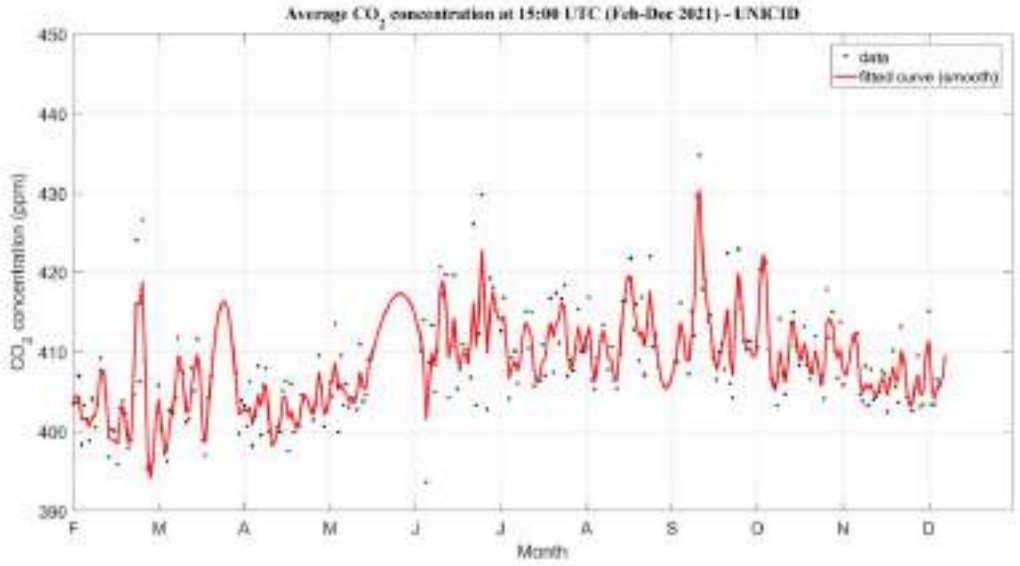

Source: author, 2023.

Figure 41 - All CO_2 concentrations obtained at 15:00 UTC (12:00 local time) from February to December, 2021 at Pico do Jaraguá.

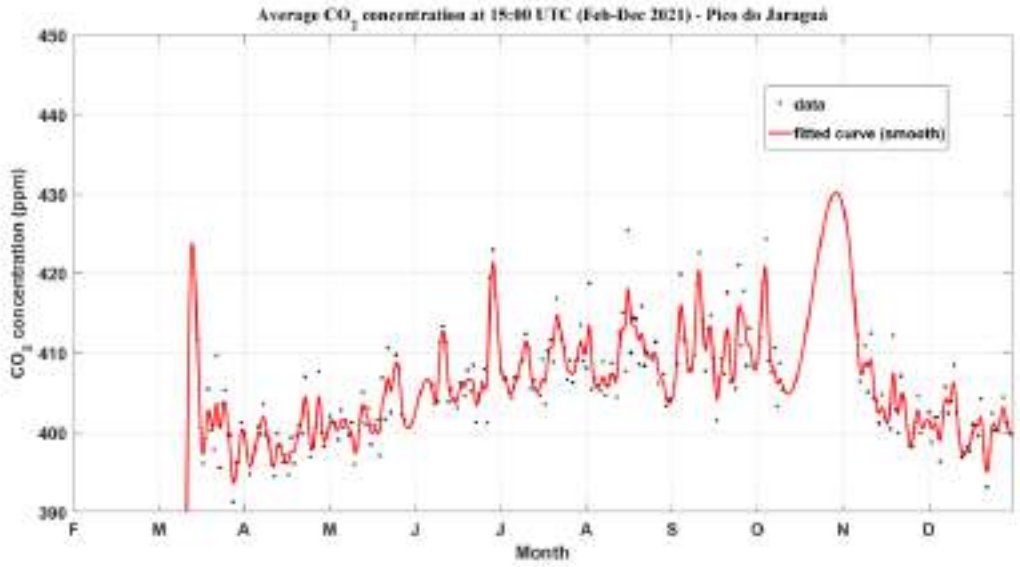

Source: author, 2023.

From figures 38-41, we see that the values obtained at 15:00 UTC show great variation from day to day, but a trend can be observed in both PBLH and CO_2 measurements. The CO_2 yearly cycle is more evident in the Pico do Jaraguá measurements, the station furthest away from the city, and less evident at IAG. Measurements from IAG station seem to show a small increase in CO_2 concentrations in the months preceding April. Although average CO_2 concentrations seem higher in March than in April at Pico do Jaraguá, it is not possible to confirm if this was also seen at Pico do Jaraguá in 2021, due to lack of data. At UNICID station, this increase from February to March can be see more clearly in Figure 36.

5.4.2 Average seasonal PBLHs and CO_2 concentrations

PBLH data from February to December 2021 was sorted into four two or three month intervals: February-March, April-June, July-September and October-December, and then averaged, in order to obtain the average seasonal PBLH cycle. These periods will be referred to as summer, fall, winter and spring, respectively. The same was done with the CO2 concentration data from IAG, UNICID and Pico do Jaraguá stations. These values are shown in figures 42-44.

Figure 42 - Diurnal averages of the PBLHs (CIENTEC) and CO_2 concentrations (IAG) obtained in four different periods: summer (in yellow), fall (in black), winter (in green), and spring (in blue).

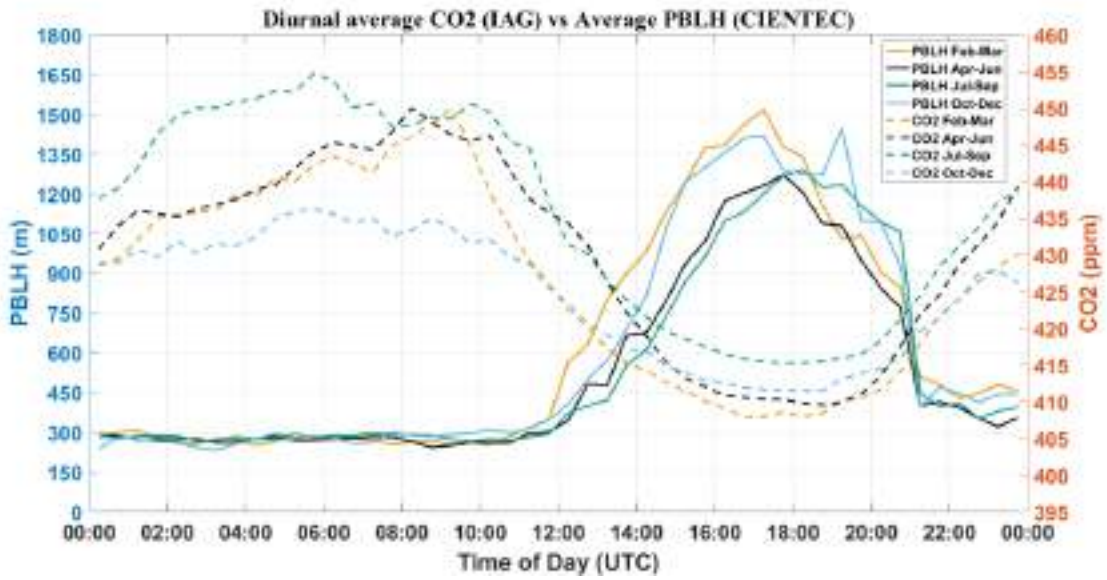

Source: author, 2023.

Figure 43 - Diurnal averages of the PBLHs (CIENTEC) and CO_2 concentrations (UNICID) obtained in four different periods: summer (in yellow), fall (in black), winter (in green), and spring (in blue).

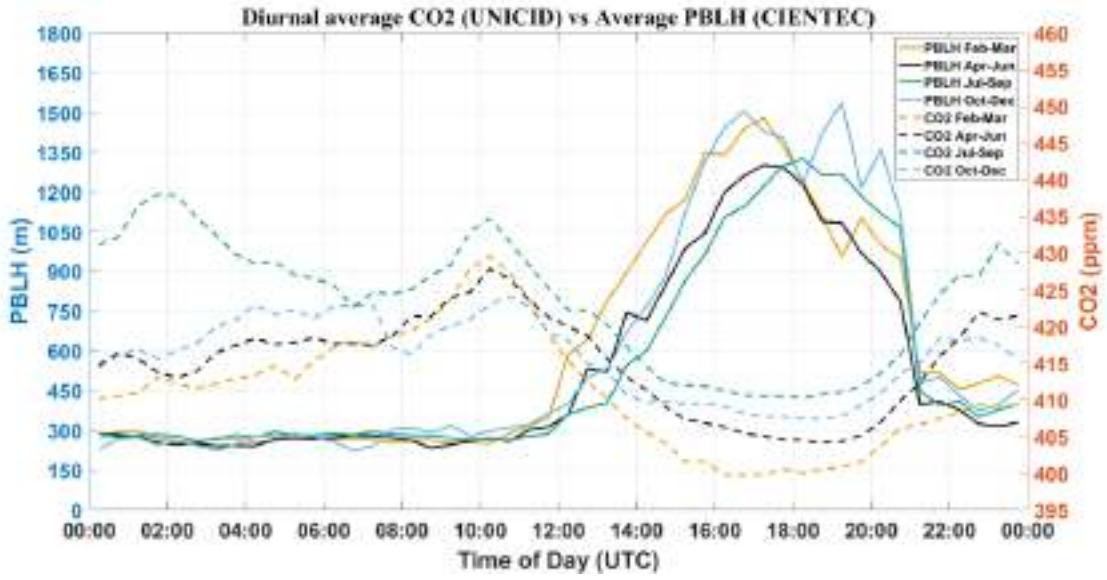

Source: author, 2023.

Figure 44 - Diurnal averages of the PBLHs (CIENTEC) and CO_2 concentrations (Pico do Jaraguá) obtained in four different periods: summer (in yellow), fall (in black), winter (in green), and spring (in blue).

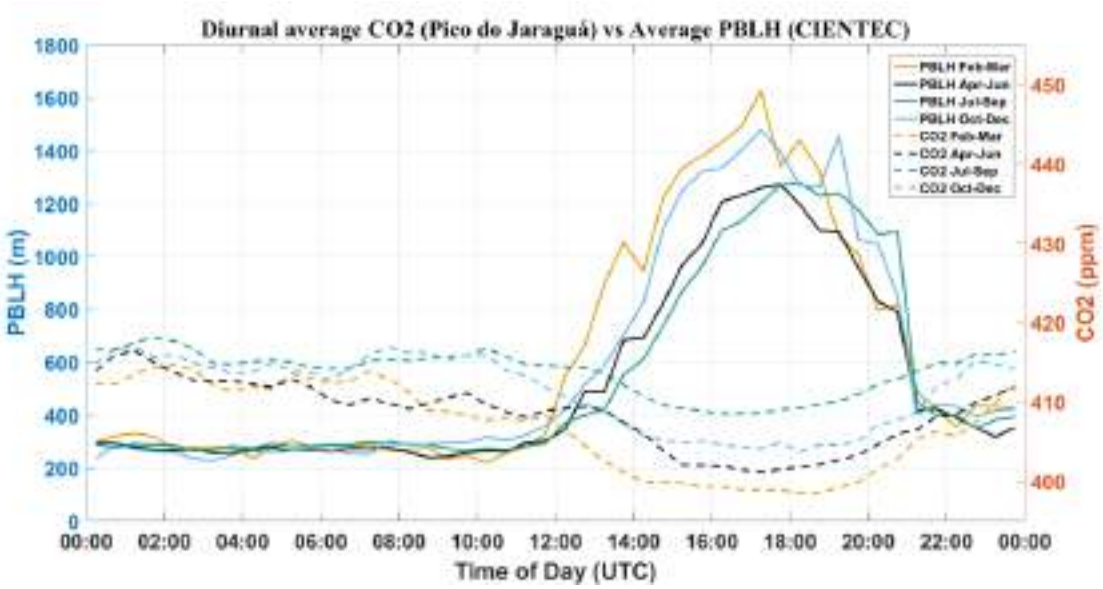

Source: author, 2023.

From figures 42-44, we see that the PBL top height was greater, and PBL growths begins earlier, in warmer months (October-March). During nighttime, CO_2 concentrations start low and quickly rise to their peak value in early morning. Fall and winter experience delayed PBL growth, reaching maximum average top height during mid-to-late afternoon.

CO_2 concentrations at IAG, UNICID and Pico do Jaraguá stations have different daily cycles. At all three stations, CO_2 concentrations are highest in winter. Lowest CO_2 concentrations vary from station to station during nighttime and early morning, but daytime concentrations are lowest during summer in all three stations. At IAG and UNICID stations, CO_2 concentrations increase during the night in spring, summer and fall, reaching their peak values in early morning. This peak is seen earlier at IAG than at UNICID. Winter CO_2 concentrations fluctuate during the night, showing two peaks instead of one. The greatest variations in daily CO_2 concentrations are seen in summer and winter. At IAG, peak CO_2 concentrations are seen earlier in summer than in winter. The CO_2 increase seen in mid-to-late afternoon is also delayed during winter. At Pico do Jaraguá station, CO_2 concentrations vary little from season to season, and values show a slow decrease during the night and early morning. A sharper decrease is seen after 12:00 UTC and minimum concentrations were obtained

during the afternoon. Average concentrations start increasing again after 18:00 UTC. The daily maximum variation was obtained in summer. All throughout the year, average CO_2 concentrations vary less than 15 ppm during the day at this station.

The results show a negative correlation between the CO_2 averages and the PBLH averages. As can be seen in Figures 42-44, the negative correlation between PBL top heights and CO2 concentrations can be seen both in their average seasonal values, but also in how their daily cycles change during the year. The elevated CO_2 concentrations measured in winter, as well as the delayed decrease in early morning and increase in later afternoon when compared to the warmer seasons, is accompanied by a lower average PBLH and delayed PBL growth and collapse. Daytime average CO_2 concentrations are lowest in summer, which is consistent with higher PBLHs during this period.

Figures 45-48 show the correlation matrices of PBLH values and CO_2 concentrations in all stations during February-March, April-June, July-September and October-December. Values closer to -1 show significant negative correlation.

Figure 45 - Correlation Matrix of PBLHs and CO_2 concentrations obtained at all stations during February-March, 2021.

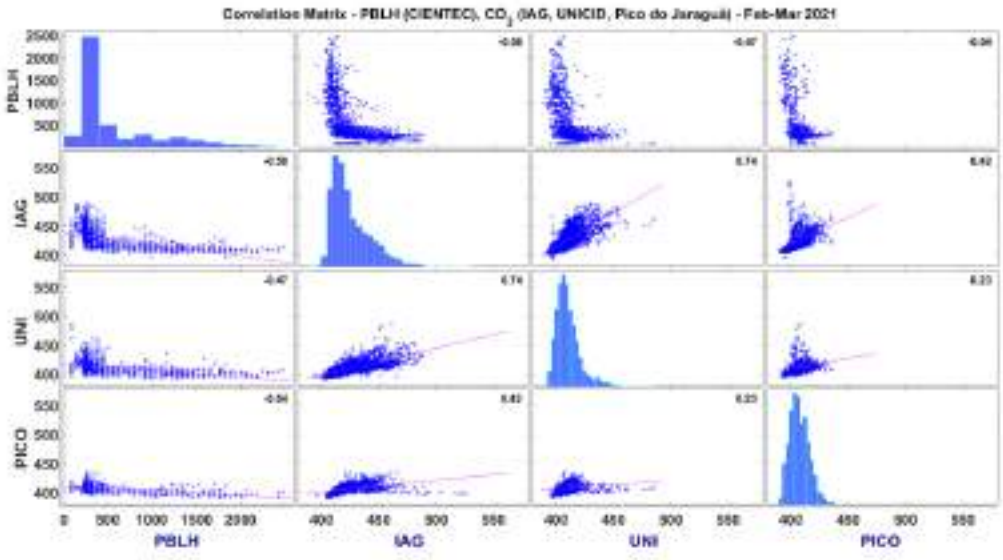

Source: author, 2023.

Figure 46 – Correlation Matrix of PBLHs and CO_2 concentrations obtained at all stations during April-June, 2021.

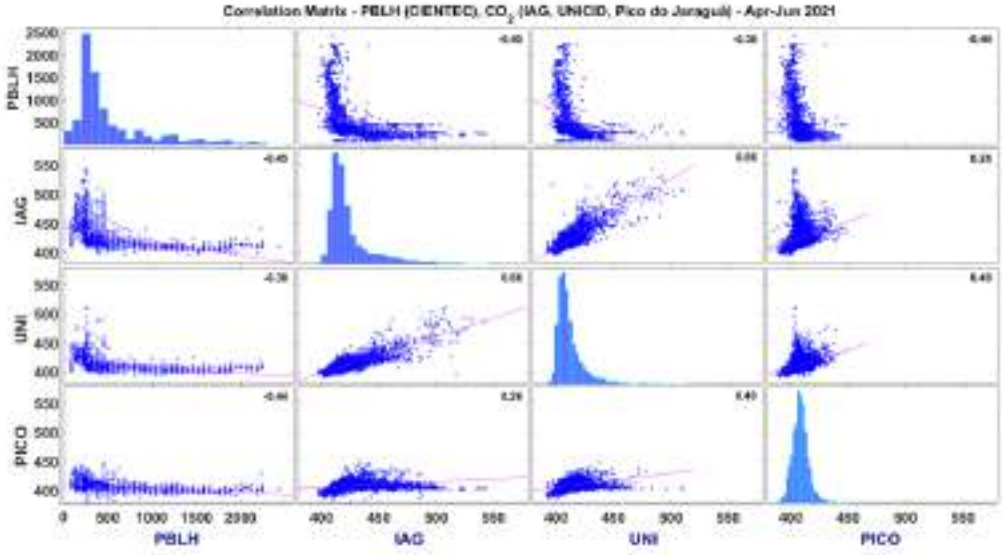

Source: author, 2023.

Figure 47 - Correlation Matrix of PBLHs and CO_2 concentrations obtained at all stations during July-September, 2021.

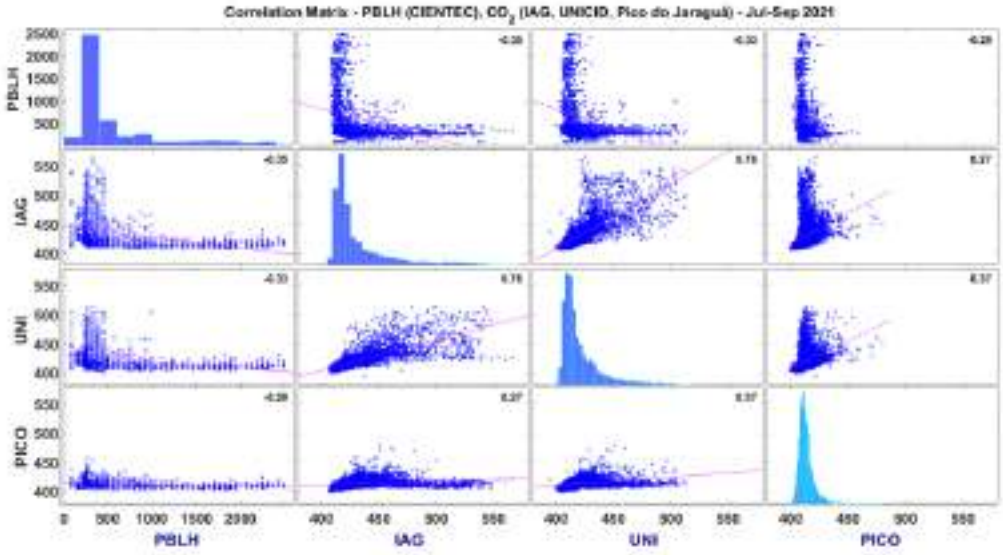

Source: author, 2023.

Figure 48 - Correlation Matrix of PBLHs and CO_2 concentrations obtained at all stations during October-December, 2021.

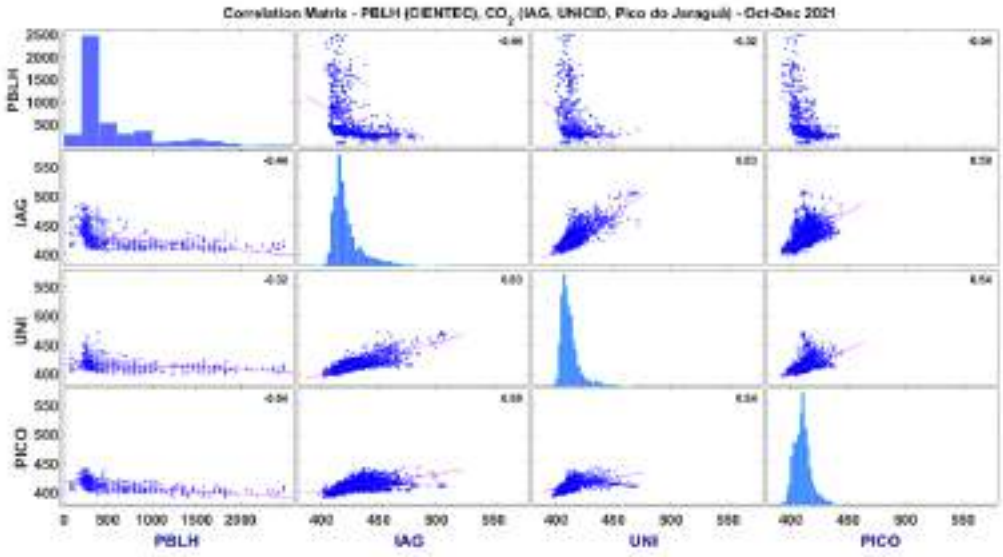

Source: author, 2023.

From figure 45-48, CO_2 concentrations obtained in all stations show negative correlation to the PBLH values obtained at CIENTEC. In summer, fall and winter, CO_2 concentrations measured at IAG show the most significant negative correlation with the corresponding PBLH values, whereas in spring, Pico do Jaraguá measurements show the most significant negative correlation, followed by IAG and UNICID measurements. The greatest negative correlation was seen in summer in all stations. Winter values show the least significant correlations in two of the three stations. Additionally, we see that correlation between IAG and UNICID stations is higher than between each of these stations and Pico do Jaraguá. The latter, being located at a higher altitude and furthest from the city, is less influenced by urban CO_2 emissions.

5.5 Case study July 24th – 26th

From July 24 to July 26, skies were mostly cloudless and the PBL growth can be easily seen. Due to the lack of precipitation and clouds, it was possible to obtain accurate PBLH values for these days. This interval was selected for a case study to analyze if the PBLH variations seen in these three days reflect similar changes in CO2 concentration values.

Figures 49, 51 and 53 show the range corrected signal obtained from ceilometer measurements in July 24-26, 2021 at CIENTEC, and figures 50, 52 and 54 show the CO2 concentrations at the three stations during the same interval.

Figure 49 - RCS measured by the CHM 15k ceilometer as a function of height and time of day (UTC) on July 24th, 2021. PBLHs obtained from the ceilometer data are shown in black.

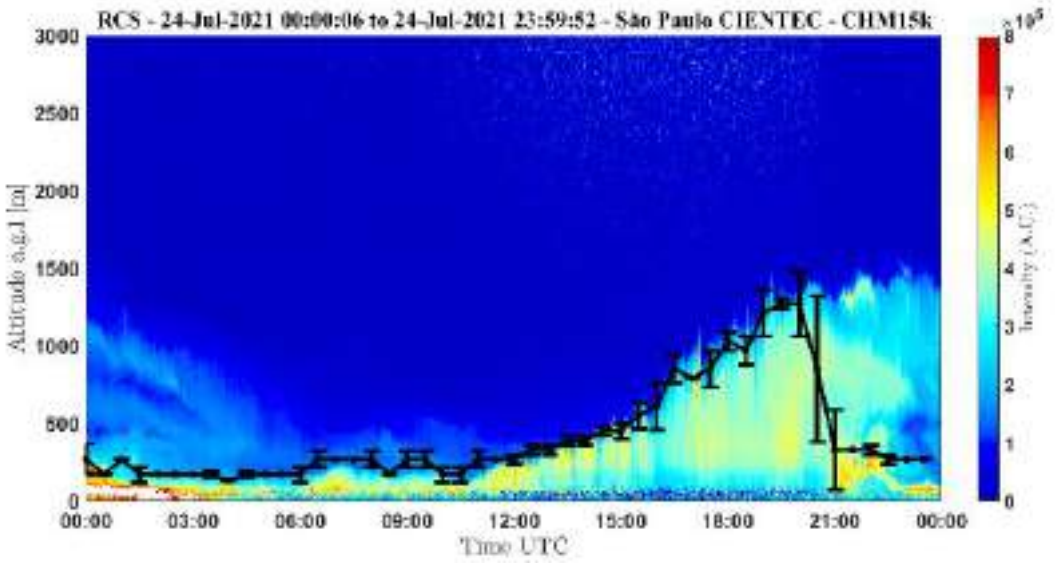

Source: author, 2023.

Figure 50 – CO_2 concentrations measured on July 24th, 2021 at the IAG, UNICID and Pico do Jaraguá stations.

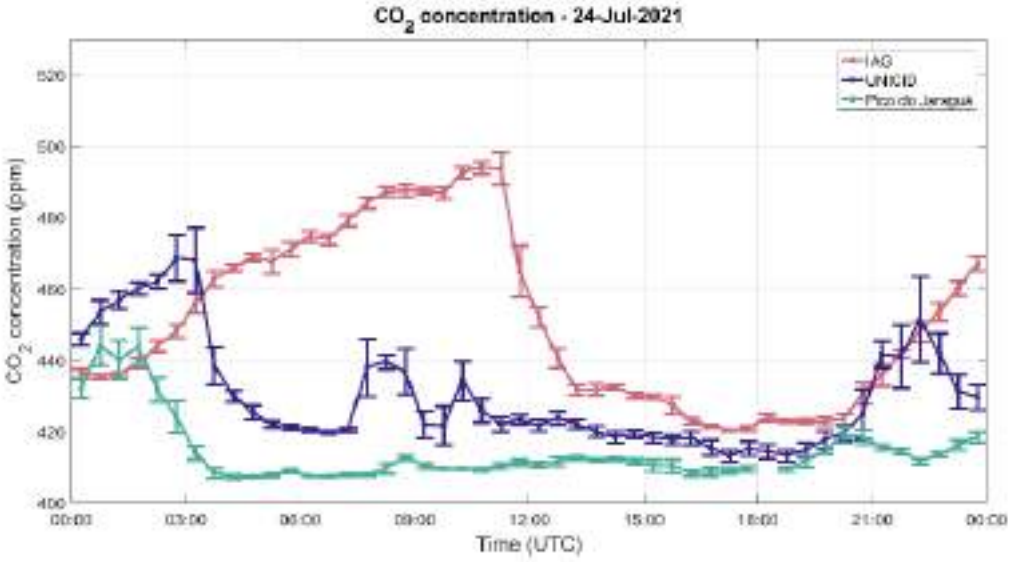

Source: author, 2023.

Figure 51 - RCS measured by the CHM 15k ceilometer as a function of height and time of day (UTC) on July 25th, 2021. PBLHs obtained from the ceilometer data are shown in black.

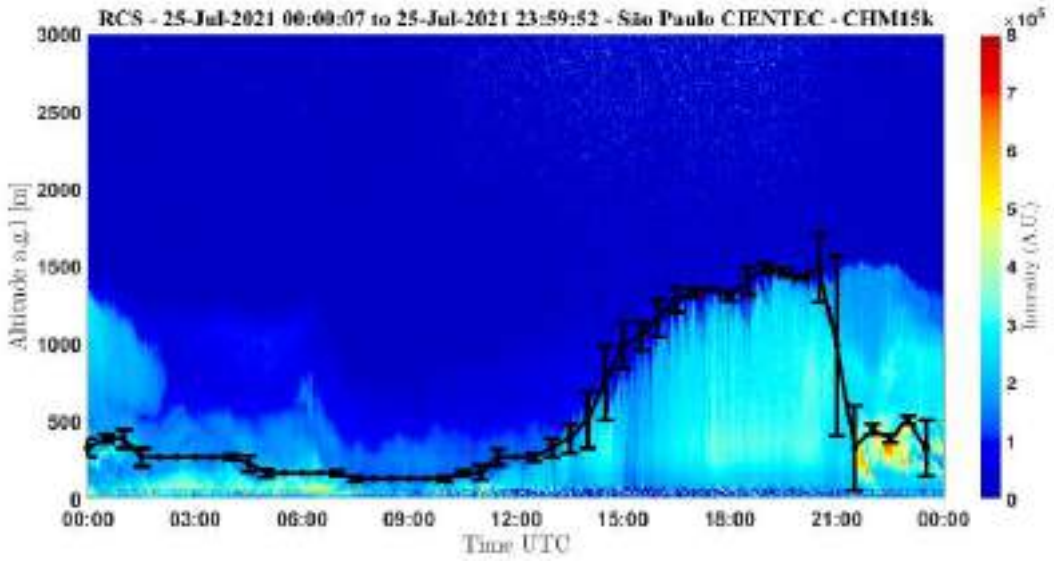

Source: author, 2023.

Figure 52 – CO_2 concentrations measured on July 25th, 2021 at the IAG, UNICID and Pico do Jaraguá stations.

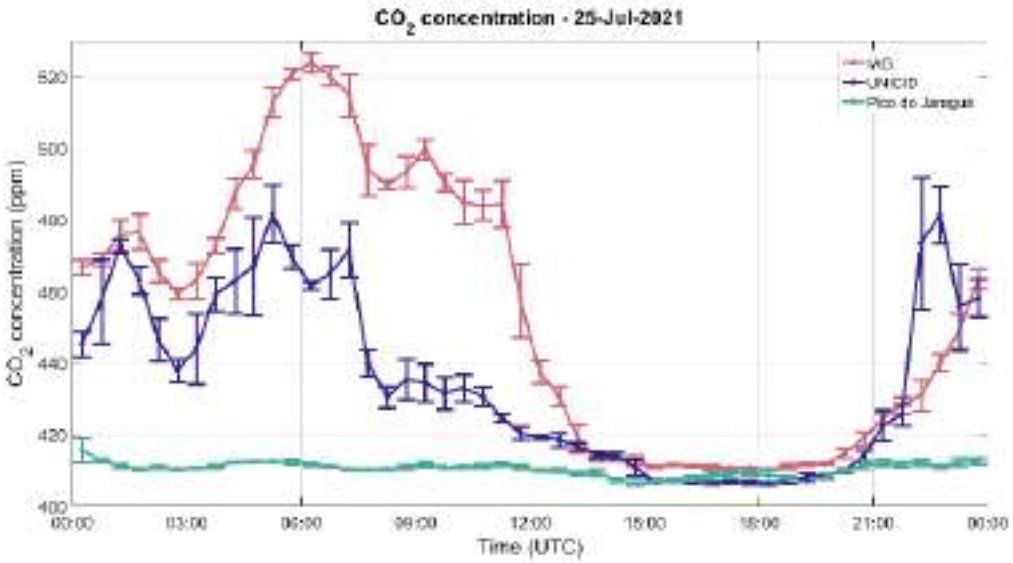

Source: author, 2023.

Figure 53 - RCS measured by the CHM 15k ceilometer as a function of height and time of day (UTC) on July 26th, 2021. PBLHs obtained from the ceilometer data are shown in black.

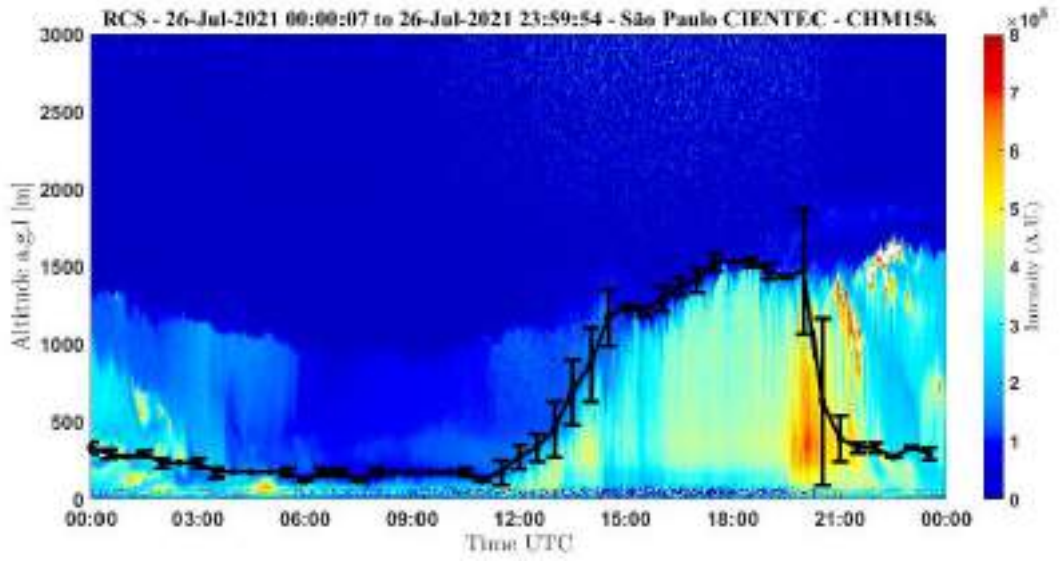

Source: author, 2023.

Figure 54 – CO_2 concentrations measured on July 26th, 2021 at the IAG, UNICID and Pico do Jaraguá stations.

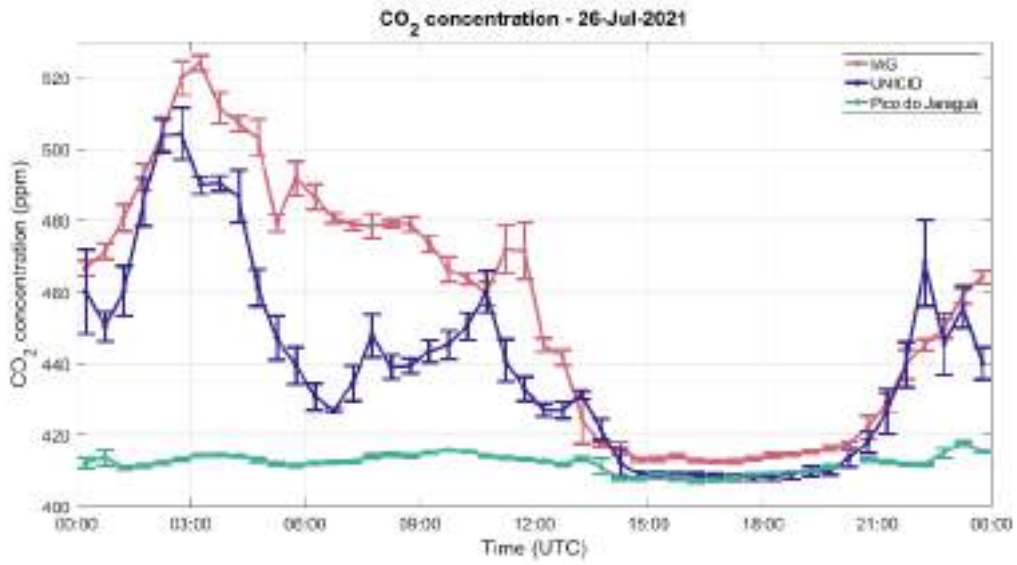

Source: author, 2023.

Figure 55 – 30-minute averaged PBLHs and CO_2 concentrations obtained on July 24th, 2021 at the CIENTEC and IAG stations.

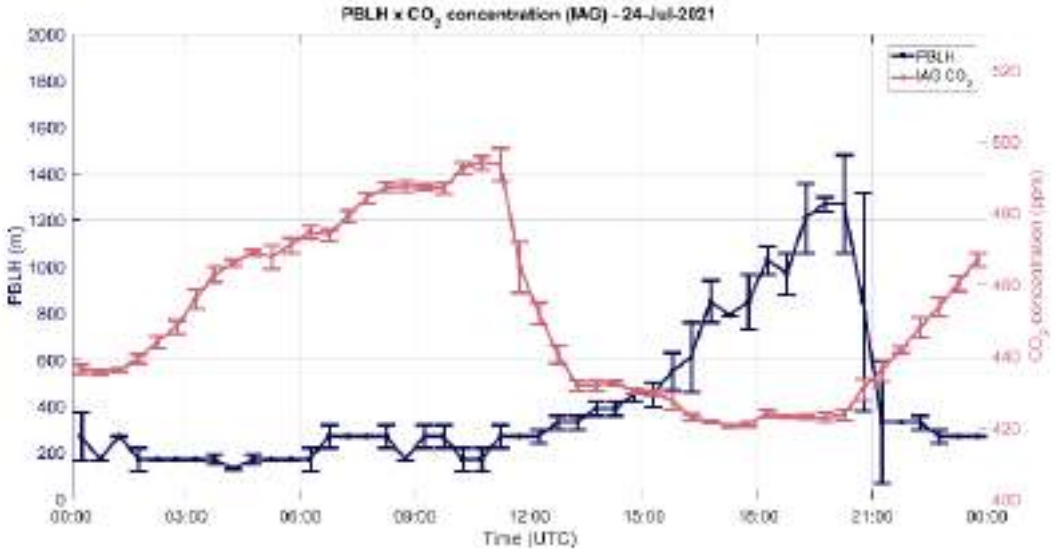

Source: author, 2023.

Figure 56 - 30-minute averaged PBLHs and CO_2 concentrations obtained on July 25th, 2021 at the CIENTEC and IAG stations.

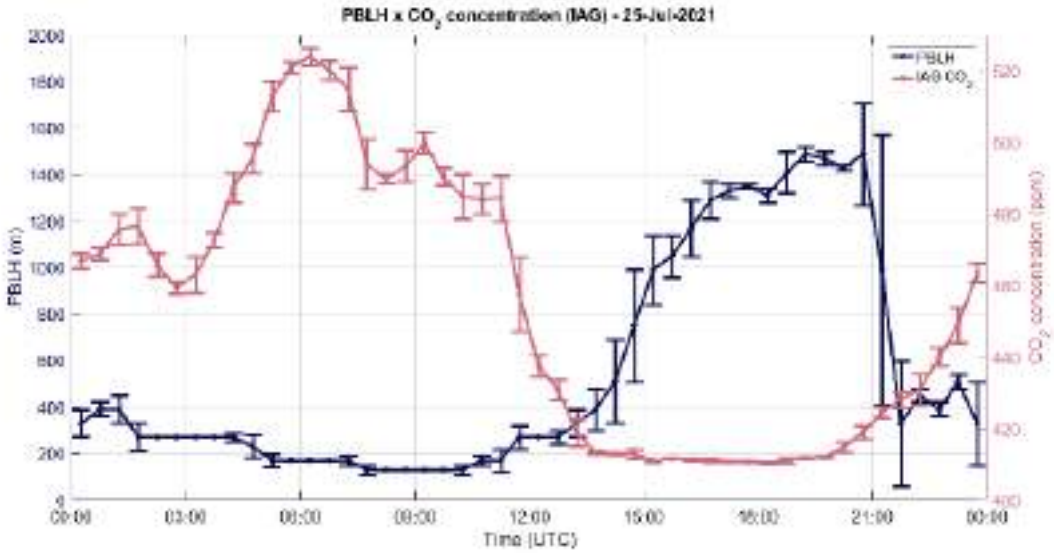

Source: author, 2023.

Figure 57 - 30-minute averaged PBLHs and CO_2 concentrations obtained on July 26th, 2021 at the CIENTEC and IAG stations.

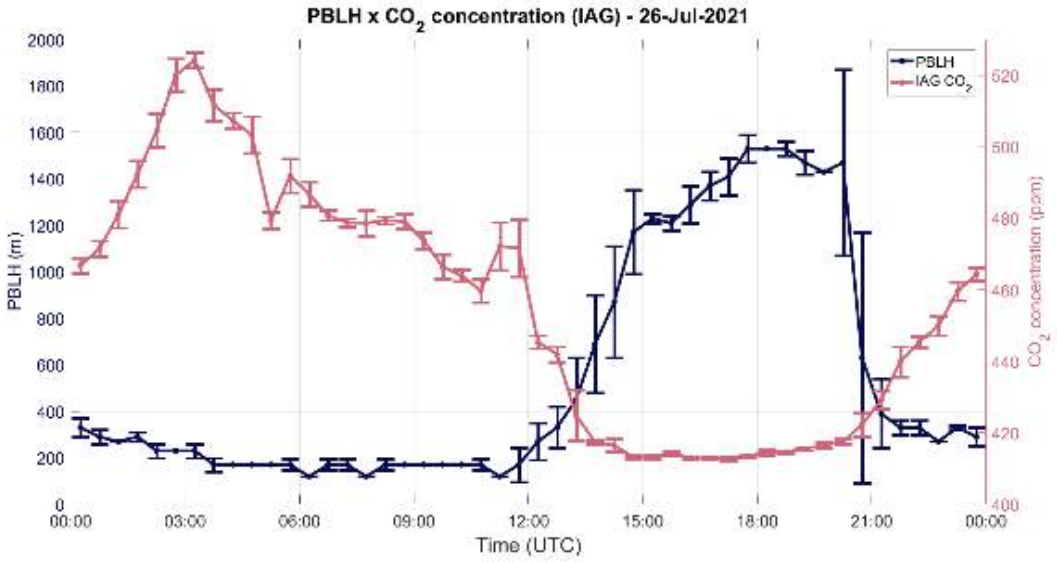

Source: author, 2023.

Maximum PBL height was reached increasingly earlier from July 24 to July 26, while PBL growth was delayed, but also sharper. Concurrently, a similar behavior was seen in the CO_2 data, with a sharp decrease in concentrations starting around 12:00 UTC on July 26 and a few minutes earlier on July 24, but minimum concentrations being reached earlier on July 26. Maximum CO_2 concentrations were measured at around 11:00 UTC on July 24, at around 06:00 am on July 25, and at around 03:00 am on July 26. Nighttime PBLH values were highest, and CO_2 concentrations lowest, on July 24. Similarly, between 12:00 UTC and 21:00 UTC, PBLH values were lowest, as well as CO2 concentrations were highest, on July 24.

Air masses arriving in the city have similar origin during the selected interval. Backward trajectories of air masses arriving on July 23 to July 26 were obtained with the NOAA Hysplit Trajectory Model, using the IAG station as a source point, and are shown in figure 58.

Figure 58 – Backward trajectories of air masses arriving at the IAG station on July 23-26, 2021.

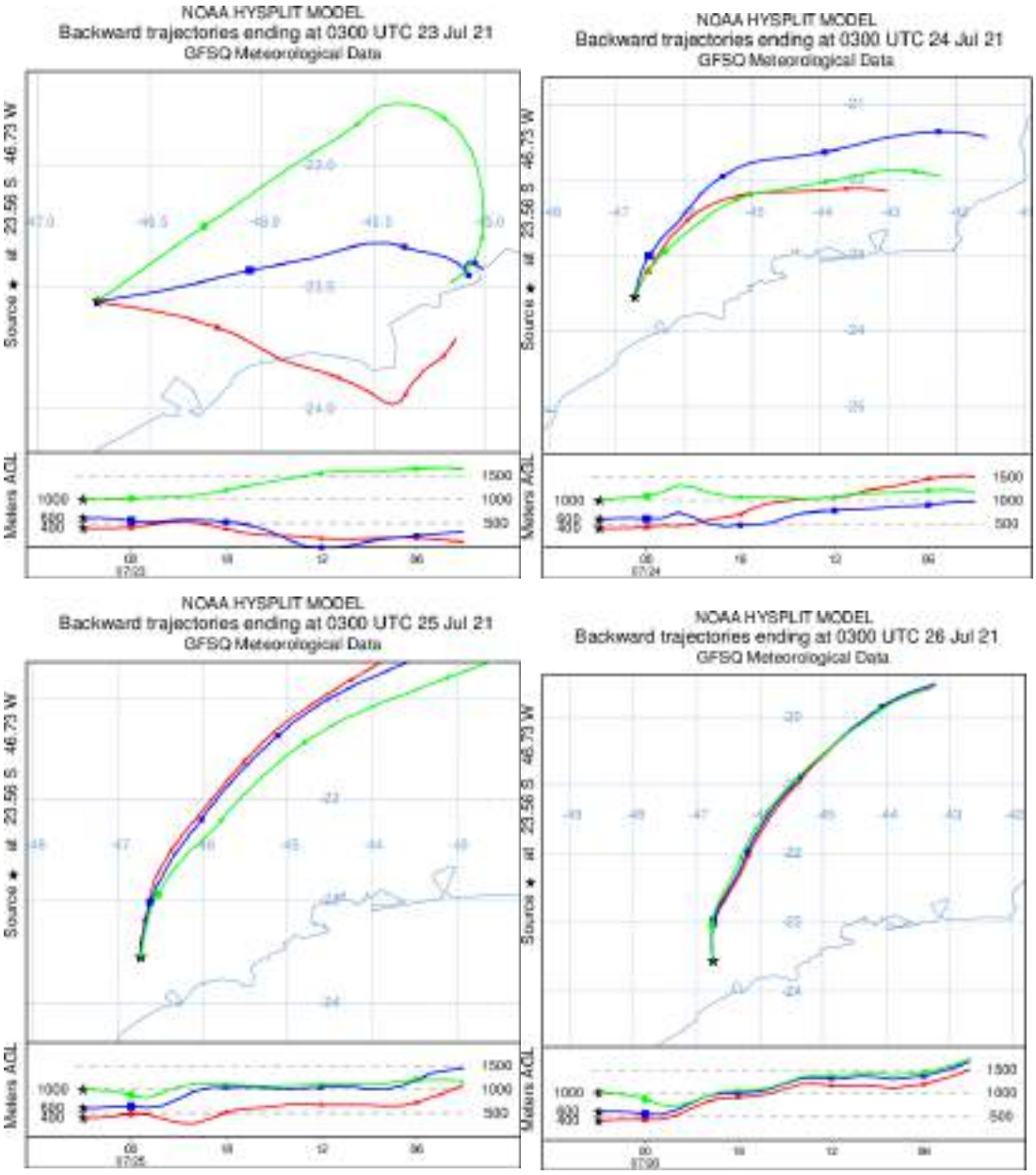

Source: Made with NOAA's Hysplit Trajectory Model, 2023.

6 CONCLUSION

This work presented the results derived from the operation of a lidar system and a ceilometer throughout 2021 at two different locations in the city of São Paulo, approximately 15 km apart. Data from lidar and ceilometer measurements were used to obtain the Planetary Boundary Layer height with the Wavelet Covariance Transform Method. Due to its weaker laser source, the ceilometer data suffers from significant signal noise and attenuation, but the instrument can be used to obtain high-quality results, similar to those obtained from more powerful lidar systems, in clear-sky situations. Similar difficulties were encountered when attempting to obtain the PBLH from data from both instruments, in the presence of clouds and aerosol layers. Three case studies were shown, comparing the PBL heights obtained with both instruments in different situations. In situations where the PBL is well defined, the WCT method obtains similar results from data of both instruments, as shown in the first case study. These results also show that PBL top height does not vary greatly between both locations. In situations such as the second case study, in which there is the presence of low clouds near the top of the PBL, the results show greater divergence between the instruments, also reflecting the different cloud distributions between the locations. In cases like this, the comparison of results is impaired. In the third case study, which shows the results for a situation in which there are aerosols layers, the aerosol layer can be misidentified as the PBL top, and the case study shows that this misidentification can happen both when using ceilometer and lidar data.

The ceilometer was shown to be a powerful tool for long-term PBLH measurements. With ceilometer data from February to December 2021, it was possible to analyse PBLH changes throughout the year, with enough data points to allow the observation of both the daily cycle and the seasonal cycle of the PBL. $PBLH_{ceil}$ averages per month were calculated, obtained from the ceilometer data. The average heights for each month vary between 800 and 1000 m for the entire period. The maximum average PBLHceil values were obtained during first and the last trimester of the year. With the ceilometer data, average PBLHceil for the entire period was obtained, with a 30-minute temporal resolution. The results show a daily cycle for the

period correspondent to the expected PBL daily cycle, with PBL growth starting in mid-to-late morning due to convective processes resulting from incident solar radiation, with the top height reaching its maximum value during the afternoon.

Long-term PBLH measurements have numerous applications, such as studies and modelling of pollutant and gas dispersion. The results obtained in this work were compared to CO_2 measurements obtained in different measurement sites in São Paulo, to observe the effect of PBL changes in CO_2 concentrations. PBLH values obtained from the ceilometer data were compared with CO_2 concentrations obtained at three measurement sites in the city: IAG, UNICID and Pico do Jaraguá. These values were averaged per month and intercomparisons at different times of the day were presented. Average PBLHs and CO_2 concentrations were also compared by season. The results show negative correlation between PBL heights and CO_2 concentrations throughout all the day, with increasing PBL heights being accompanied by decreasing CO_2 concentrations, and this behavior was seen throughout the year. Seasonal variations were seen in the average PBL heights and CO_2 concentrations, with the highest PBLHs and lowest CO_2 concentrations being obtained during summer, followed by spring, fall and winter. PBL growth was delayed during the period correspondent to fall and winter (April-June and July-September), and a corresponding delayed decrease in CO_2 concentrations was also observed in the same period. PBLH values obtained from July 24, 2021 to July 26, 2021 were compared to the CO_2 concentrations in the same period. These days were chosen due to the absence of clouds and rainfall. The results show that day-to-day changes in PBL behavior are accompanied by similar changes in the CO_2 measurements, with higher nighttime PBL heights being accompanied by lower CO_2 concentrations, and lower maximum daytime PBL heights corresponding to higher CO_2 concentrations during the day. Changes in PBL growth timing, such as an earlier or quicker development of the Mixed Layer, also reflected changes seen in the CO_2 data, with sharpest PBL growth being accompanied by minimum CO_2 concentrations being measured at an earlier time. These results show the negative correlation between PBL top heights and CO_2 concentrations, similarly to what was seen in the monthly and seasonal intercomparisons.

REFERENCES

ANGELINE F., BARNABA F., LANDI C. T., CAPORASO L., GOBBI P.G. Study of atmospheric aerosols and mixing layer by lidar. ***Radiation Protection Dosimetry***, 275-279, 2009.

ARELLANO, J. V.-G., GIOLI, B., MIGLIETTA, F., JONKER, H. J. J., BALTINK, H. K., HUTJES, R. W. A., AND HOLTSLAG, A. A. M.: Entrainment process of carbon dioxide in the atmospheric boundary layer, ***Journal of Geophysical Research***, 109, 2004.

BAARS, H., ANSMANN, A., ENGELMANN, R., ALTHAUSEN, D. Continuous monitoring of the boundary-layer top with lidar. ***Atmospheric Chemistry and Physics***, 7281 – 7296, 2008.

BALLANTYNE, A.P., ALDEN, C.B., MILLER, J.B., TANS, P.P., WHITE, J.W.C.: Increase in observed net carbon dioxide uptake by land and oceans during the past 50 years. ***Nature***, 488, 70–7, 2012.

BIANCO, L., DJALALOVA, I. V., KING, C. W., WILCZAK, J. M.: Diurnal evolution and annual variability of boundary-layer height and its correlation to other meteorological variables in California's Central Valley, ***Boundary Layer Meteorology***, 140, 491–511, 2011.

BITTER, M., BALL, S. M., POVEY, I. M., JONES, R. L.: A broadband cavity ringdown spectrometer for in-situ measurements of atmospheric trace gases, ***Atmospheric Chemistry and Physics,*** 5, 2547–2560, 2005.

BRAVO-ARANDA, J. A., MOREIRA, G. de A., NAVAS-GUZMÁN, F., GRANADOS-MUÑOZ, M. J., GUERRERO-RASCADO, J. L., POZO-VÁSQUEZ, D., ARBIZU-BARRENA, C. A new methodology for PBL height estimations based on lidar depolarization measurements: analysis and comparison against MWR and WRF model-based results. ***Atmospheric Chemistry and Physics***, 6839–6851, 2017.

BROOKS, I. M. Finding boundary layer top: Application of a wavelet covariance transform to lidar backscatter profiles. ***Journal of Atmospheric And Oceanic Technology***, 1092 – 1105, 2003.

CAICEDO, V., RAPPENGLÜCK, B., LEFER, B., MORRIS, G., TOLEDO, D., DELGADO, R.: Comparison of aerosol lidar retrieval methods for boundary layer height detection using ceilometer aerosol backscatter data. ***Atmos. Chem. Phys***., 10, 1609–1622, 2017.

CANADELL, J. G., CIAIS, P., DHAKAL, S., DOLMAN, H. (A.J.), FRIEDLINGSTEIN, P., GURNEY, K., HELD, A., JACKSON, R., LE QUÉRÉ, C., MALONE, E., OJIMA, D., PATWARDHAN, A., PETERS, G., RAUPACH, M.: Interactions of the carbon cycle, human activity, and the climate system: A research portfolio. ***Current Opinion in Environmental Sustainability***, 2. 301-311, 2010.

CARVALHO, V. S. B., FREITAS, E. D., MARTINS, L. D., M, J. A., MAZZOLI, C. R., ANDRADE, M. F.: Air quality status and trends over the Metropolitan Area of São Paulo, Brazil as a result of emission control policies, ***Environmental Science & Policy***, 47, 68-79, 2015.

COHN S. A., ANGEVINE W. A., Boundary layer height and entrainment zone thickness measured by lidars and wind-profiling radars. ***Journal of Applied. Meteorology,*** 1233-1247, 2000.

CIMINI, D., ANGELIS, F., DUPONT, J.-C., Pal, S., HAEFFELIN, M.: Mixing layer height retrievals by multichannel microwave radiometer observations***. Atmos. Meas. Tech***., 6, 2941–2951, 2013.

CROSSON, E.R.: A cavity ring-down analyzer for measuring atmospheric levels of methane, carbon dioxide, and water vapor. ***Applied Physics B***, 92, 403–408, 2008.

CULF, A., FISCH, G., MALHI, Y., AND NOBRE, C.: The influence of the atmospheric boundary layer on carbon dioxide concentrations over a tropical forest, ***Agricultural and Forest Meteorology***, 85, 149– 158, 1997.

DAVIS, K. J., GAMAGE, N., HAGELBERG, C. R., KIEMLE, C., LENSCHOW, D. H., SULLIVAN, P. P. An Objective Method for Deriving Atmospheric Structure from Airborne Lidar Observations. ***Journal of Atmospheric and Oceanic Technology***, 17, 1455-1468, 2000.

DAYAN U., LIFSHITZ-GOLDEN B., PICK K. Spatial and structural variation of the atmospheric boundary layer during summer in Israel-profiler and rawinsonde measurements, ***Journal of Applied Meteorology***, 447-457, 2002.

EICHINGER, W. E., HOLDER, H. E., KNIGHT, R., NICHOLS, J., COOPER, D. I., HIPPS, L. E., KUSTAS, W. P., PRUEGER, J. H.: Lidar Measurement of Boundary Layer Evolution to Determine Sensible Heat Fluxes, ***Journal of Hydrometeorology***, 6, 840–853, 2005.

EMEIS, S., SCHÄFER, K., MÜNKEL, C.: Surface-based remote sensing of the mixing - layer height - a review. ***Meteorologische Zeitschrift***, 621 – 630, 2008.

FLAMANT, C., PELON, J., FLAMANT, P.; DURAND, P.: Lidar determination of the entrainment zone thickness at the top of the unstable marine atmospheric boundary layer. ***Boundary-Layer Meteorology,*** 83, 247–284, 1997.

GARRATT, J. R. Review: the atmospheric boundary layer. ***Earth-Science Reviews***, 89 – 134, 1994.

GLICKMAN, T. ***Glossary of Meteorology***. American Meteorological Society, Boston, MA, 2000.

GRANADOS-MUÑOZ, M. J., NAVAS-GUZMÁN, F., BRAVO-ARANDA, J. A., GUERRERO-RASCADO, J. L., LYAMANI, H.,FERNÁNDEZ-GÁLVEZ, J., AND ALADOS-ARBOLEDAS, L. Automatic determination of the planetary boundary layer height using lidar: One-year analysis over southeastern Spain, ***Journal of Geophysical Research***, 117, 2012.

HODNEBROG, Ø., AAMAAS, B., FUGLESTVEDT, J.S., MARSTON, G., MYHRE, G., NIELSEN, C.J., SANDSTAD, M., SHINE, K.P., WALLINGTON, T.J.: Updated Global Warming Potentials and Radiative Efficiencies of Halocarbons and Other Weak Atmospheric Absorbers. ***Reviews of Geophysics***, 58, 1-30, 2020

IPCC: ***Climate Change 2014: Synthesis Report***. Contribution of Working Groups I, II and III to the Fifth Assessment Report of the Intergovernmental Panel on Climate Change [Core Writing Team, R.K. Pachauri and L.A. Meyer (eds.)], 151 pp, IPCC, Geneva, Switzerland, 2014. Disponível em: <https://www.ipcc.ch/report/ar5/syr/> Acesso em 15 mar. 2022.

IPCC: ***Climate Change 2021: The Physical Science Basis***. Contribution of Working Group I to the Sixth Assessment Report of the Intergovernmental Panel on Climate Change [Masson-Delmotte, V., P. Zhai, A. Pirani, S.L. Connors, C. Péan, S. Berger, N. Caud, Y. Chen, L. Goldfarb, M.I. Gomis, M. Huang, K. Leitzell, E. Lonnoy, J.B.R. Matthews, T.K. Maycock, T. Waterfield, O. Yelekçi, R. Yu, and B. Zhou (eds.)]. Cambridge University Press, Cambridge, United Kingdom and New York, NY, USA, pp. 3−32, 2021.

JACOBS, C. M. J., AND DE BRUIN, H. A. R.: The Sensitivity of Regional Transpiration to Land-Surface Characteristics: Significance of Feedback***, Journal of Climate***, 5(7), 683-698, 1992.

KAIMAL, J. C. AND FINNIGAN, J. J.: 1994, ***Atmospheric boundary layer flows: their structure and measurement***, Oxford Univ. Press, New York, 289 pp, 1994.

KIM, J. AND VERMA, S.B.: Carbon dioxide exchange in a temperate grassland ecosystem. ***Boundary-Layer Meteorology***. 52:135-149, 1990.

KIRSCHKE, S., BOUSQUET, P., CIAIS, P., SAUNOIS, M., CANADELL, J. G., DLUGOKENCKY, E. J., BERGAMASCHI, P., BERGMANN, D., BLAKE, D. R. , BRUHWILER, L., CAMERON-SMITH, P., CASTALDI, S. , CHEVALLIER, F., FENG, L., FRASER, A., HEIMANN, M., HODSON, E. L., HOUWELING, S., JOSSE, B., FRASER, P. J., KRUMMEL, P.B., LAMARQUE, J.-F., LANGENFELDS, R.L., LE QUÉRÉ, C., NAIK, V., O'DOHERTY, S., PALMER, P.I., PISON, I., PLUMMER, D., POULTER B., PRINN, R.G., RIGBY, M., RINGEVAL, B., SANTINI, M., SCHMIDT, M., SHINDELL, D.T. , SIMPSON, I.J., SPAHNI, R., STEELE, L.P., STRODE, S.A., SUDO, K., SZOPA, S., VAN DER WERF, G.R., VOULGARAKIS, A., VAN WEELE, M., WEISS, R.F., WILLIAMS, J.E., ZENG, G.: Three decades of global methane sources and sinks. ***Nature Geoscience***., 6, 813-823, 2013.

KORNOHEN, K., GIANNAKAKI, E, MIELONEN, T., PFÜLLER, A., LAAKSO, L., VAKKARI, V., BAARS, H, ENGELMANN, R; BEUKES, J., ZYL, P.G.; RAMANDH, A; NTSANGWANE, L, JOSIPOVIC, M., TIITTA, P., FOURIE, G., NGWANA, I., CHILOANE, K., KOMPPULA, M. Atmospheric boundary layer top height in South Africa: measurements with lidar and radiosonde compared to three atmospheric models. ***Atmospheric Chemistry and Physics***. 14(8), 4263-4278, 2013.

HAEFELE, A.. The E-PROFILE/TOPROF network of automatic lidars and ceilometers for profiling of aerossol and volcanic ash, 28th Int. Laser Radar Conf. **Proceedings**, 2017.

HAEFFELIN, M., ANGELINI, F., MORILLE, Y., MARTUCCI, G., FREY, S., GOBBI, G. P., LOLLI, S., O'DOWD, C. D., SAUVAGE, L., XUEREF-REMY, I, WASTINE, B., FEIST, D.G. Evaluation of mixing-height retrievals from automatic profiling lidars and ceilometers in view of future integrated networks in Europe. ***Boundary-Layer Meteorology.*** 143, 49-75, 2012.

HAYDEN, K.L., Jw, H.R.S., BOTTENHEIM, J.W., Fa, W.H.F., MARTIN, J.B., STEYN, D.G. The vertical chemical and meteorological structure of the boundary layer in the lower fraser valley during pacific 93**.** ***Atmospheric Environnment,*** 31 (14), 2089–2105, 1997.

HOLTON, J. R., PYLE, J., CURRY, J. A. ***Encyclopedia of Atmospheric Sciences***. Elsevier Science Ltd, 2002.

HOOPER, W. P., ELORANTA, E. W.: Lidar measurements of wind in the planetary boundary layer: the method, accuracy, and results from joint measurements with radiosonde and kytoon. ***Journal of Applied Metereology and Climatology***, 25, 990-1001, 1986.

INSTITUTO BRASILEIRO DE GEOGRAFIA E ESTATÍSTICA (IBGE): Available in: <https://cidades.ibge.gov.br/brasil/sp/panorama > Accessed on January 24th 2021.

JACKSON, R. B., SAUNOIS, M., BOUSQUET, P., CANADELL, J. G., POULTER, B., STAVERT, A. R., BERGAMASCHI, P., NIWA, Y., SEGERS, A., TSURUTA, A.: Increasing anthropogenic methane emissions arise equally from agricultural and fossil fuel sources. ***Environmental Research Letters***, 15(7), 2020.

KORHONEN, K., GIANNAKI, E., MIELONEN, T., PFÜLLER, A., LAAKSO, L., VAKKARI, V., BAARS, H., ENGELMANN, 28 R., BEUKES, J. P., VAN ZYL, P. G., RAMANDH, A., NTSANGWANE, L., JOSIPOVIC, M., TIITA, P., FOURIE, G., NGWANA, I., CHILOANE, K., KOMPPULA, M. Atmospheric boundary layer top height in South Africa: 30 measurements with lidar and radiosonde compared to three atmospheric models. ***Atmospheric Chemistry and Physics***., 31 14(8), 4263–4278, 2014.

KOVALEV, V. A., AND EICHINGER, W. E***.: Elastic LIDAR - Theory, Practice and Analysis Methods.*** John Wiley & Sons, 2004.

LI, H., YANG, Y., HU, X.-M., HUANG, Z., WANG, G., ZHANG, B., ZHANG, T. Evaluation of retrieval methods of daytime convective boundary layer height based on lidar data, ***Journal of Geophysical Research: Atmospheres,*** 122, 4578– 4593, 2017.

LIU, S., LIANG, X.Z. Observed diurnal cycle climatology of planetary boundary layer height. ***Journal of Climate,*** 23, 5790–5809, 2010.

LOPES, F. J. S., MOREIRA, G. A., RODRIGUES, P. F., GUERRERO-RASCADO, J. L., ANDRADE, M. F., LANDULFO, E. Comparison between two algorithms based on diferente wavelets to obtain the planetary boundary layer height. SPIE 9246, Lidar Technologies, Techniques, and Measurements for Atmospheric Remote Sensing, 92460H, ***Proceedings***, 2014.

MAHRT, L., SUN, J., BLUMEN, W., DELANY, A. C.& ONCLEY, S: Nocturnal Boundary-Layer Regimes. ***Boundary-Layer Meteorology*** 88, 255–278, 1998.

MARTUCCI, G., MATTHEY, R., MITEV, M., RICHNER, H. Comparison between Backscatter Lidar and Radiosonde Measurements of the Diurnal and Nocturnal Stratification in the Lower Troposphere. **Journal of Atmospheric and Oceanic Technology*.,*** 24, 1231–1244, 2007.

MEDEIROS, B., HALL, A.D., STEVENS, B. What Controls the Mean Depth of the PBL. ***Journal of Climate***, 18, 3157-3172, 2005.

MENUT, L., FLAMANT, C., PELON, J., and FLAMANT, P. H. Urban boundary-layer height determination from lidar measurements over the Paris area, ***Applied Optics,*** 38, 6, 945–954, 1999.

MOREIRA, G. A., GUERRERO-RASCADO, J.L., BRAVO-ARANDA, J.A., BENAVENT-OLTRA, J.A, ORTIZ-AMEZCUA, P. RÓMAN, R., BEDOYA-VELÁSQUEZ, A. E., LANDULFO, E., ALADOS-ARBOLEDAS, L.: Study of the planetary boundary layer by microwave radiometer, elastic lidar and Doppler lidar estimations in Southern Iberian Peninsula, ***Atmos.Res***., 213, pp. 185-195, 2018.

MÜNKEL, C., ERESMAA, N., RÄSÄNEN, J., KARPPINEN, A. Retrieval of mixing height and dust concentration with lidar ceilometer. ***Boundary-Layer Meteorology***, 2007

OLIVEIRA, A. P., BORNSTEIN R. D., SOARES, J.: Annual and Diurnal Wind Patterns in the City of São Paulo. ***Water, Air, & Soil Pollution***, 3, 3-15, 2003.

PAL, S., BEHRENDT, A., WULFMEYER, V.: Elastic-backscatter-lidar-based characterization of the convective boundary layer and investigation of related statistics. In ***Annales Geophysicae***, 2010.

PAL, S., HAEFFELIN, M. Forcing mechanisms governing diurnal, seasonal, and interannual 9 variability in the boundary layer depths: Five years of continuous lidar observations over a suburban site 10 near Paris. ***Journal of Geophysical Research: Atmospheres,*** 120, 11,936–11,956, 2015.

PENG et al. Ceilometer-based analysis of Shanghai's boundary layer height (under rain-free and fog-free conditions). **Journal of Atmospheric and Oceanic Technology*.*** 34, 749-764, 2017.

PIIRONEN, A. K., ELORANTA, E. W. Convective boundary layer depths and cloud geometrical properties obtained from volume imaging lidar data, ***Journal of Geophysical Research,*** 100, 569–576, 1995.

RAMANATHAN, V., CICERONE, R. J., SINGH, H. B., AND KIEHL, J. T.: Trace gas trends and their potential role in climate change, ***Journal of Geophysical Research***., 90(D3), 5547– 5566, 1985.

RIBEIRO, F. N. D., OLIVEIRA, A. P., SOARES, J., MIRANDA, R. M., BARLAGE, M., CHEN, F.: Effect of sea breeze propagation on the urban boundary layer of the metropolitan region of Sao Paulo, Brazil, ***Atmospheric Research***, 214, 174-188, 2018.

SEIBERT P., BEYRICH, F., GRYNING, S. E., JOFFRE, S., RASMUSSEN, A., TECIER, P. Review and intercomparison of operational methods for the determination of the mixing height, ***Atmospheric Environment***. 34, 1001–1027, 2000.

STULL, R. B. ***An Introduction to Boundary Layer Meteorology.*** Kluwer Academic Publishers, 1988.

TANG G., ZHU X., HU B., XIN J., WANG L., MÜNKEL C., MAO G. and WANG Y.: Vertical variations of aerosols and the effects responded to the emission control: application of lidar ceilometer in Beijing during APEC, 2014, ***Atmospheric Chemistry and Physics***, 13173-13209, 2015.

TANG, G., ZHANG, J., ZHU, X., SONG, T., MÜNKEL, C., HU, B.. Mixing layer height and its implications for air pollution over beijing, China. ***Atmospheric Chemistry and Physics***, 2459–2475, 2016.

TROEN, I. B., MAHRT, L.: A simple model of the Atmospheric Boundary Layer; sensitivity to surface evaporation. ***Boundary-Layer Meteorology***, 37, 129–148, 1986.

UNEP: The Emissions Gap Report 2018, ***United Nations Environment Programme***, Nairobi, 2018.

UNITED NATIONS, World urbanization prospects: The 2014 revision - highlights, Statistical Papers - United Nations (Ser. A), ***Population and Vital Statistics Report***, UN, New York, 2014.

VOULGARAKIS, A., NAIK, V., LAMARQUE, J.-F., SHINDELL, D. T., YOUNG, P. J., PRATHER, M. J., WILD, O., FIELD, R. D., BERGMANN, D., CAMERONSMITH, P., CIONNI, I., COLLINS, W. J., DALSØREN, S. B., DOHERTY, R. M., EYRING, V., FALUVEGI, G., FOLBERTH, G. A., HOROWITZ, L. W., JOSSE, B., MACKENZIE, I. A., NAGASHIMA, T., PLUMMER, D. A., RIGHI, M., RUMBOLD, S. T., STEVENSON, D. S., STRODE, S. A., SUDO, K., SZOPA, S., AND ZENG, G: Analysis of present day and future OH and methane lifetime in the ACCMIP simulations. ***Atmospheric Chemistry and Physics***, 13, 2563-2587, 2013.

WALLACE, J. M., HOBBS, P. ***Atmospheric Science - An Introductory Survey***. 2nd Edition, International Geophysics Series, Vol. 92, Academic Press, USA, 2006.

WANG, J., BRAS, R. L., ELTAHIR, E. A. B.: The Impact of Observed Deforestation on the Mesoscale Distribution of Rainfall and Clouds in Amazonia, ***Journal of Hydrometeorology***, 1(3), 267-286, 2000.

WEITKAMP, C. ***Lidar: Range-Resolved Optical Remote Sensing of the Atmosphere, Springer Series in Optical Sciences***, 102, New York: Springer, 2005.

WERNER E., SIEGRIST, F.: The influence of nocturnal CO2 advection on CO2 flux measurements, ***Basic and Applied Ecology***, Vol. 1(2), 177-188, 2000.

WIEGNER, M., EMEIS, S., FREUDENTHALER, V., HEESE, B., JUNKERMANN W., MÜNKEL, C., SCHÄFER K., SEEFELDNER, M., VOGT, S.: Mixing layer height over Munich, Germany: Variability and comparisons of different methodologies, ***Journal of Geophysical Research,*** 111, D13201, 2006.

WMO: ***Greenhouse Gas Bulletin (GHG Bulletin) - No.17: The State of Greenhouse Gases in the Atmosphere Based on Global Observations through 2020***, 67 pp., Geneva, 2021.

INSTITUTO DE PESQUISAS ENERGÉTICAS E NUCLEARES
Diretoria de Pesquisa, Desenvolvimento e Ensino
Av. Prof. Lineu Prestes, 2242 – Cidade Universitária CEP: 05508-000
Fone/Fax(0XX11) 3133-8908
SÃO PAULO – São Paulo – Brasil
http://www.ipen.br

O IPEN é uma Autarquia vinculada à Secretaria de Desenvolvimento, associada à Universidade de São Paulo e gerida técnica e administrativamente pela Comissão Nacional de Energia Nuclear, órgão do Ministério da Ciência, Tecnologia, Inovações e Comunicações.